SPECIAL
OWLeS
COLLECTION

Characterizing and Constraining Uncertainty Associated with Surface and Boundary Layer Turbulent Fluxes in Simulations of Lake-Effect Snowfall

JUSTIN R. MINDER AND W. MASSEY BARTOLINI

University at Albany, State University of New York, Albany, New York

CHRISTOPHER SPENCE AND NEWELL R. HEDSTROM

Environment and Climate Change Canada, Ottawa, Ontario, Canada

PETER D. BLANKEN

University of Colorado Boulder, Boulder, Colorado

JOHN D. LENTERS

University of Wisconsin–Madison, Madison, Wisconsin

(Manuscript received 19 July 2019, in final form 7 January 2020)

ABSTRACT

Lake-effect snow (LeS) storms are driven by strong turbulent surface layer (SL) and planetary boundary layer (PBL) fluxes of heat and moisture caused by the flow of cold air over relatively warm water. To investigate the sensitivity of simulated LeS to the parameterization of SL and PBL turbulence, high-resolution simulations of two major storms, downwind of Lakes Superior and Ontario, are conducted using the Weather Research and Forecasting Model. Multischeme and parameter sensitivity experiments are conducted. Measurements of overlake fluxes and downwind snowfall are used to evaluate the simulations. Consistent with previous studies, LeS is found to be strongly sensitive to SL and PBL parameterization choices. Simulated precipitation accumulations differ by up to a factor of 2 depending on the schemes used. Differences between SL schemes are the dominant source of this sensitivity. Parameterized surface fluxes of sensible and latent heat can each vary by over 100 W m^{-2} between SL schemes. The magnitude of these fluxes is correlated with the amount of downwind precipitation. Differences between PBL schemes play a secondary role, but have notable impacts on storm morphology. Many schemes produce credible simulations of overlake fluxes and downwind snowfall. However, the schemes that produce the largest surface fluxes produce fluxes and precipitation accumulations that are biased high relative to observations. For two SL schemes studied in detail, unrealistically large fluxes can be attributed to parameter choices: the neutral stability turbulent Prandtl number and the threshold friction velocity used for defining regimes in the overwater surface roughness calculation.

1. Introduction

Lake-effect snow (LeS) storms occur when cold air is advected over relatively warm lake water. The resulting vertical temperature and moisture gradients drive strong turbulent surface sensible heat and moisture fluxes. These fluxes moisten and destabilize the boundary layer, leading to the formation of convective clouds, often shallow in depth, which may be organized into different morphologies by boundary layer and mesoscale circulations (e.g., LeMone 1973; Hjelmfelt 1990; Niziol et al. 1995; Veals and Steenburgh 2015; Laird et al. 2017). LeS storms, and similar sea-effect snow storms, occur downwind of many bodies of water around the world (e.g., Estoque and Ninomiya 1976; Niziol et al. 1995; Kindap 2010; Laird et al. 2009; Alcott et al. 2012; Laird et al. 2016) and produce some of the world's largest snowfall totals (Burt 2007). Some of the most

Corresponding author: Justin R. Minder, jminder@albany.edu

DOI: 10.1175/WAF-D-19-0153.1

intense and impactful LeS storms occur downwind of the Great Lakes of North America where LeS has a dominant influence on seasonal snowfall (Eichenlaub and Hodler 1979; Veals and Steenburgh 2015).

A recent example of the societal impact of LeS storms occurred from 17 to 21 November 2014 when storms spawned by Lake Erie buried parts of the Buffalo, New York, region under up to 223 cm of snowfall. These storms resulted in at least 14 deaths, hundreds of roof collapses, closure of Interstate-90, and deployment of the National Guard (Vermette 2015). Damage and cleanup costs were estimated at $49 million (U.S. dollars) and resulted in a declaration of a major disaster by the federal government (Federal Emergency Management Agency 2014). The National Weather Service (NWS) forecast was generally skillful; however, there were key shortcomings including an underestimation of snowfall rates by a factor of 2 on 17 November and errors in prediction of the storm's position during the night of 18–19 November. These errors highlight that forecasting and understanding these storms remains a major challenge.

High-resolution numerical simulations provide a powerful tool for improving prediction and understanding of LeS. Simulations with convection-permitting resolution—horizontal grid spacing less than about 5 km, where convective clouds are treated explicitly instead of parameterized—have proven capable of resolving many of the key features of LeS storms (Ballentine et al. 1998; Steenburgh and Onton 2001; Tripoli 2005; Maesaka et al. 2006; Alcott and Steenburgh 2013; Wright et al. 2013; McMillen and Steenburgh 2015a; Campbell and Steenburgh 2017; Bergmaier et al. 2017; Mulholland et al. 2017), but also can exhibit biases in storm intensity, location, and morphology (e.g., Ballentine et al. 1998; McMillen and Steenburgh 2015a). The skill of LeS storm simulations is limited in part by uncertainties in atmospheric initial and boundary conditions (Saslo and Greybush 2017), lake surface conditions (Zhao et al. 2012), and the parameterization of both cloud microphysics (Reeves and Dawson 2013; McMillen and Steenburgh 2015b; Saslo and Greybush 2017) and near-surface turbulent fluxes (Conrick et al. 2015; Saslo and Greybush 2017; Fujisaki-Manome et al. 2017).

Here we focus on uncertainties in simulations of LeS storms associated with turbulent fluxes in the surface layer (SL) and planetary boundary layer (PBL). Conrick et al. (2015) investigated the sensitivity to SL and PBL parameterization schemes in the Weather Research and Forecasting (WRF) Model for a major LeS event downwind of Lake Erie. They found differences in simulated maximum storm-total liquid-equivalent precipitation that exceeded 20 mm over a 6-h period (exceeding a factor of 2). These were primarily attributed to large contrasts in the simulated overlake surface sensible heat fluxes F_H and latent heat fluxes F_Q, with lake-averaged F_H and F_Q differing by more than 400 W m^{-2} across schemes. Schemes with higher fluxes produced greater low-level instability, stronger convection, and more intense snowfall. They attributed the variations in fluxes across schemes to choices in the SL schemes regarding the value of the turbulent Prandtl number and the formulation of the similarity stability functions. However, direct evaluation of the schemes was not possible due to a lack of overlake measurements of turbulent fluxes.

Several previous studies have used airborne eddy covariance observations to directly measure near-surface turbulent fluxes during Great Lake LeS events (Lenschow 1973; Chang and Braham 1991; Kristovich 1993; Kristovich et al. 2003; Gerbush et al. 2008). The studies report large fluxes and large event-to-event variability over open water (F_H = 50–320 W m^{-2}, F_Q = 70–250 W m^{-2}) and much smaller fluxes in the presence of partial lake-ice cover (F_H, $F_Q \sim$ 0–10 W m^{-2}). While valuable, these measurements are temporally limited, only providing data during cross-lake transects flown by instrumented aircraft.

More recently, eddy covariance measurements of fluxes have been collected from surface deployments in the Great Lakes (e.g., Blanken et al. 2011; Spence et al. 2013; Shao et al. 2015). Fujisaki-Manome et al. (2017) used such measurements to evaluate the parameterization of turbulent fluxes in a suite of numerical models for the aforementioned November 2014 Lake Erie LeS event. They found large differences between models, with differences in peak F_H exceeding 250 W m^{-2}. All models appeared to substantially overpredict the fluxes at Long Point, the site of the midlake observations. The precise cause of the differences between models is difficult to diagnose, as models differed in their grid spacing, boundary conditions, and SL turbulence schemes.

Here we expand on these previous studies by further characterizing the sensitivity of convection-permitting LeS storm simulations to near-surface turbulence parameterization and by better constraining these sensitivities using observations. Following Conrick et al. (2015), we conduct controlled model sensitivity experiments by systematically varying SL and PBL schemes, but consider a wider range of schemes. We also test the robustness of the results by considering two events over different lakes and with different storm morphologies. For one event downwind of Lake Superior, we follow the methods of Fujisaki-Manome et al. (2017) and use eddy covariance measurements of surface fluxes to evaluate our simulations, but, due to our experimental design, are able to more precisely attribute some of the sources of biases and differences across schemes. For another event downwind

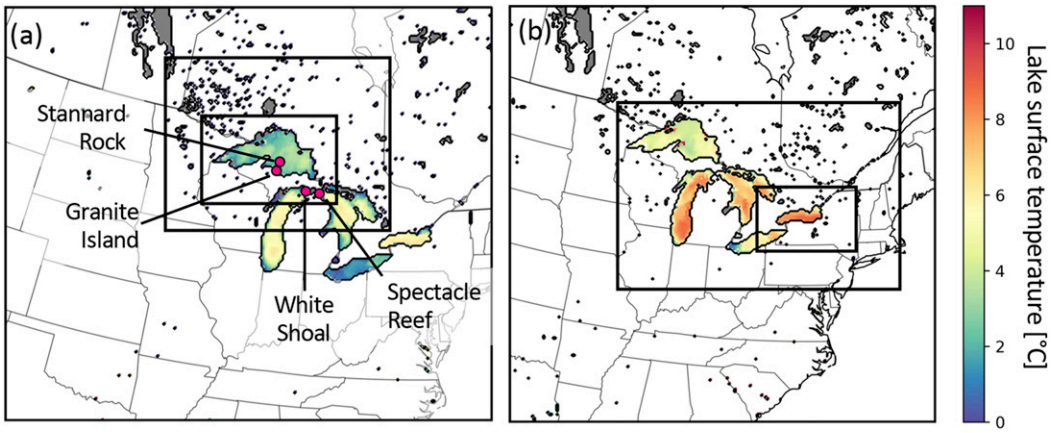

FIG. 1. Maps showing computational domains and lake surface temperature for WRF simulations for (a) Case 1, 10–13 Feb 2016, and (b) Case 2, 11 Dec 2013. For each panel, the full extent shows the outermost domain, while black rectangles denote the inner domains. Lake surface temperature is shaded according to the color bar with locations of lake ice cover shaded in gray. Locations of GLEN stations used for flux measurements are marked with pink circles and labeled in (a).

of Lake Ontario, we make use of high-quality snowfall observations from a recent field campaign to further constrain the simulations.

2. Data and methods

Two contrasting LeS cases are simulated at convection-permitting resolution using a numerical weather prediction model. Case 1 is a multiday event that occurred downwind of Lake Superior from 10 to 13 February 2016 with widespread snowfall. Case 2 is a single-day event that occurred downwind of Lake Ontario on 11 December 2013 and produced isolated but very intense snowfall. For each case, experiments are conducted to explore the sensitivity of the simulation to the methods used to parameterize SL and PBL turbulence. Model simulations are evaluated against observations from standard operational datasets as well as specialized research datasets to quantify variations in model skill and physical realism.

a. WRF simulations

The above-described cases are simulated using the Advanced Research version of WRF Model (Skamarock et al. 2008). The two events are simulated with slightly different versions of WRF: Case 1 is simulated using version 3.9.1.1, while Case 2 is simulated using version 3.9.0. For each case, a control simulation and a series of sensitivity experiments are conducted.

1) CONTROL CONFIGURATION

The baseline configuration used for our control simulation includes three two-way nested domains, with horizontal grid spacings of $\Delta x = 12$, 4, and 1.33 km, centered on the region of interest (Fig. 1). A total of 51 terrain-following sigma levels are used, with 15 within the lowest 3 km above the surface. The first level is spaced about 7 m above the surface and vertical grid spacing ranges from 20 m near the surface to 520 m aloft. Atmospheric initial and lateral boundary conditions (ICs/BCs) are taken from the NOAA Rapid Refresh (RAP; Benjamin et al. 2016) analyses, accessed from NOAA/NCEP (2012). Analyses are used instead of forecasts to minimize simulation errors associated with BCs in order to focus on errors associated with near-surface turbulence parameterization. Additionally, above the boundary layer on the outermost domain, grid nudging is used to relax simulated wind, temperature, geopotential height, and humidity toward the analyses. Simulations are initialized at 0000 UTC 10 February 2016 for Case 1 and at 1200 UTC 10 December 2013 for Case 2.

Because the archived RAP analyses did not include the land surface fields required for initialization, we used soil moisture and temperature fields from the NCEP North American Model (NOAA/NCEP 2004) to provide land surface ICs. Bottom BCs over the lakes, namely lake-surface temperature and ice concentration, are prescribed based on ''nowcast'' analyses from the NOAA Great Lakes Operational Forecast System (Chu et al. 2011; NOAA/NOS 2005). For simplicity, these lake conditions are fixed over the duration of the simulation, as only very modest changes in lake conditions occurred during the cases studied.

The choices of physical parameterizations are based on version 3 of the High-Resolution Rapid Refresh (HRRR) model (Benjamin et al. 2016, https://rapidrefresh.noaa.gov/hrrr/). The RUC scheme (Smirnova et al. 2016) is used to

TABLE 1. Summary of model configurations for the multiphysics sensitivity experiments. The PBL and SL schemes used are noted, with references included as footnotes. For PBL schemes, the type is noted: prognistic TKE or *K*-profile parameterization (KPP). For SL schemes the value of P_R and the water roughness formulation are noted.

Experiment	PBL scheme	PBL type	SL scheme	P_R	Roughness
MYNN	Mellor–Yamada–Nakanishi–Niino level 2.5[a]	TKE	MYNN	1	From COARE[b,c]
QNSE	Quasi-normal scale elimination[d]	TKE	QNSE	0.72	From[e]
MYJ	Mellor–Yamada–Janjić[f]	TKE	MYJ	1	From[e]
YSU_MM5	Yonsei University[g]	KPP	Revised MM5[h]	1	From COARE (but $\alpha = 0.0185$)[b,c]
TEMF	Total energy–mass flux[i]	TKE	TEMF	0.69	$z_o = z_{o,h} = z_{o,q} = 0.1$ mm
BOLA_MM5	Bougeault–Lacarrère[j]	TKE	Revised MM5[h]	1	From COARE (but $\alpha = 0.0185$)[b,c]
SH_MM5	Shin–Hong[k]	KPP	Revised MM5[h]	1	From COARE (but $\alpha = 0.0185$)[b,c]
ACM	Asymmetric convective model 2[l]	KPP	Pleim and Xiu[m]	0.95	$z_o = z_{o,h} = z_{o,q}$ from[n]
UW_MM5	University of Washington[o]	TKE	Revised MM5[h]	1	From COARE (but $\alpha = 0.0185$)[b,c]
GBM_MM5	Grenier–Bretherton–McCaa[p]	TKE	Revised MM5[h]	1	From COARE (but $\alpha = 0.0185$)[b,c]
MYNN_MM5	Mellor–Yamada–Nakanishi–Niino level 2.5[a]	TKE	Revised MM5[h]	1	From COARE (but $\alpha = 0.0185$)[b,c]
ACM_MM5	Asymmetric convective model[l]	KPP	Revised MM5[h]	1	From COARE (but $\alpha = 0.0185$)[b,c]

[a] Nakanishi and Niino (2004, 2009)
[b] Edson et al. (2013)
[c] Fairall et al. (2003)
[d] Mellor and Yamada (1982), Janjić (2001), and Sukoriansky et al. (2005)
[e] Janjić (1994)
[f] Mellor and Yamada (1982) and Janjić (1994, 2001)
[g] Hong et al. (2006)
[h] Jiménez et al. (2012)
[i] Angevine et al. (2010)
[j] Bougeault and Lacarrere (1989)
[k] Shin and Hong (2015)
[l] Pleim (2007)
[m] Pleim (2006)
[n] Charnock (1955)
[o] Bretherton and Park (2009)
[p] Grenier and Bretherton (2001)

simulate the evolution of the land surface. The RRTMG scheme (Iacono et al. 2008) is used for shortwave and longwave radiation. The Thompson aerosol-aware scheme (Thompson et al. 2008; Thompson and Eidhammer 2014) is employed for clouds and precipitation microphysics. Other recent modeling studies show relatively good performance using earlier versions of the Thompson scheme to simulate LeS downwind of Lake Ontario (Campbell and Steenburgh 2017) and the Great Salt Lake (McMillen and Steenburgh 2015b). Cumulus convection is parameterized on the outermost domain, using the Grell–Freitas scheme (Grell et al. 2014) and is treated explicitly on the inner domains.

PBL turbulence is parameterized using the WRF Model's default configuration of the Mellor–Yamada–Nakanishi–Niino 2.5-level (MYNN) scheme (Nakanishi and Niino 2004, 2009). Some attributes of this scheme are summarized in Table 1. This is a local scheme with a 1.5-order closure that prognoses turbulent kinetic energy (TKE). The version used here incorporates updates to the original scheme implemented as part of the development of the HRRR model, including revisions to the mixing length formulation and representation of subgrid boundary layer clouds (e.g., Benjamin et al. 2016).

SL turbulence is parameterized by the MYNN's accompanying SL scheme. Over water, surface fluxes of momentum, sensible heat, and latent heat are predicted using bulk formulas according to

$$\tau = -C_m \rho_a u^2, \tag{1}$$

$$F_H = C_h \rho_a c_p u(\theta_o - \theta), \quad \text{and} \tag{2}$$

$$F_Q = L_v C_q \rho_a u(q_o - q), \tag{3}$$

where ρ_a is the density of air, u is horizontal wind speed, θ is potential temperature, and q is water vapor mixing ratio, all at the height of the lowest model grid cell z. Both θ_o and q_o correspond to values at the surface. The term c_p is the specific heat of air at constant pressure, and L_v is the latent heat of vaporization. The transfer coefficients C_m, C_h, and C_q are parameterized using

Monin–Obukhov theory (Monin and Obukhov 1954; Foken 2006) as follows:

$$C_m = \frac{\kappa^2}{\left[\ln\left(\frac{z + z_o}{z_o}\right) - \psi_m\right]^2}, \tag{4}$$

$$C_h = \frac{u_* \kappa}{P_R u\left[\ln\left(\frac{z + z_{o,h}}{z_{o,h}}\right) - \psi_h\right]}, \quad \text{and} \tag{5}$$

$$C_q = \frac{u_* \kappa}{P_R u\left[\ln\left(\frac{z + z_{o,q}}{z_{o,q}}\right) - \psi_q\right]}, \tag{6}$$

where $u_* = \sqrt{\tau/\rho_a}$ and κ is the von Kármán constant (assumed to = 0.4). Here P_R is the turbulent Prandtl number, the ratio of the eddy diffusivities of momentum and heat, under conditions of neutral stratification. It is assumed to equal unity. The dimensionless similarity stability functions for momentum, heat, and moisture are given by ψ_m, ψ_h, and ψ_q, respectively. The momentum, thermal, and moisture roughness lengths are given by z_o, $z_{o,h}$, and $z_{o,q}$, respectively.

Over water, z_o is calculated as a function of wind speed and u_* as in the Coupled Ocean–Atmosphere Response Experiment (COARE) 3.5 bulk flux algorithm (Edson et al. 2013) with a wind speed dependent Charnock (1955) coefficient. The terms $z_{o,h}$ and $z_{o,q}$ are calculated as an empirical function of the roughness Reynolds number (Fairall et al. 2003), following the COARE 3.5/4.0 formulation. The terms ψ_m, ψ_h, and ψ_q are calculated following (Högström 1996), but with coefficients chosen to match Dyer and Hicks (1970), as a function of z, L, and surface roughness.

2) MULTISCHEME SENSITIVITY EXPERIMENTS

For each case, sensitivity experiments are conducted by rerunning the simulation with the same configuration as above, but using different SL and/or PBL turbulence parameterizations. A summary of the schemes (and their acronyms) used in these experiments, with associated references, is found in Table 1. In WRF, only certain PBL and SL schemes are compatible with each other. Several of the PBL schemes have specific corresponding SL schemes. Where this is the case, we pair those SL and PBL schemes together (MYNN, QNSE, MYJ, TEMF, ACM). For PBL schemes that do not have their own corresponding SL scheme (YSU, BOLA, SH, UW, GBM), we use the revised MM5 SL scheme (Jiménez et al. 2012). To help separate the sensitivity to PBL and SL scheme, we also run experiments where the MYNN scheme is paired with the revised MM5 surface layer. Additionally, due to problems with simulations crashing when using the ACM PBL with its native SL scheme, we ran ACM with the revised MM5 SL for Case 2.

The experiments encompass a range of SL and PBL parameterization approaches. Selected attributes of the schemes are summarized in Table 1. Some PBL schemes use K-profile parameterizations (KPP) that parameterize the eddy diffusivity K based on PBL depth and an assumed profile shape. Others use 1.5-order closures that parameterize K based on prognosed turbulent kinetic energy (TKE). The PBL schemes also differ in their applications of local versus nonlocal approaches to mixing (e.g., Cohen et al. 2015). These variations in PBL scheme formulation have been found to have large impacts on PBL structure and convective storms (e.g., Coniglio et al. 2013; García-Díez et al. 2013; Cohen et al. 2015; Milovac et al. 2016).

All the SL schemes considered here use formulations based on Monin–Obukhov theory but differ in their precise formulations. For instance, differing expressions for the empirical similarity stability functions ψ are used, drawing from a range of expressions found in the literature (e.g., Foken 2006). The schemes also differ in their choice of P_R, with values ranging from 0.69 to 1, again reflecting uncertainty found in the literature (e.g., Foken 2006; Li 2019). Another source of difference is the treatment of roughness lengths over water. The two schemes with the simplest representation use the same values for z_o, $z_{o,h}$, and $z_{o,q}$, either a constant value of 0.1 mm (TEMF) or based on Charnock (1955) (ACM). The QNSE and MYJ schemes follow Janjić (1994), calculating roughness differently in three different viscous sublayer regimes. For the "rough with spray" regime, defined as $u_* > 0.7\ \mathrm{m\ s^{-1}}$, the viscous sublayer is neglected and $z_o = z_{o,h} = z_{o,q}$, with values given by Charnock (1955). For the "rough" regime, $0.225\ \mathrm{m\ s^{-1}} < u_* < 0.7\ \mathrm{m\ s^{-1}}$, only $z_{o,h}$, $z_{o,q}$ are modified to account for viscous sublayer effects, while for the "smooth" regime, $u_* < 0.225\ \mathrm{m\ s^{-1}}$, z_o, $z_{o,h}$, and $z_{o,q}$ are all modified. Similar to MYNN, the revised MM5 scheme uses a roughness formulation based on COARE, but with a fixed Charnock (1955) coefficient of 0.0185.

b. Observations

1) SNOWFALL

Surface snowfall observations are compared with simulated snowfall for both cases. For the first case, we consider daily observations of accumulated snow depth S and liquid equivalent precipitation P from the Global Historical Climatology Network (GHCN; Menne et al. 2012a,b). GHCN integrates observations from numerous networks and applies standard quality assurance checks.

However, caution should be exercised in the interpretation of these data as many of the stations may be subject to substantial undercatch of frozen precipitation (e.g., Rasmussen et al. 2012). For Case 2, which occurred during the Ontario Winter Lake-effect Systems field campaign (OWLeS; Kristovich et al. 2017), we take advantage of high-quality manual observations of S and P, which were taken in sheltered locations at 6-h intervals on snow boards that were wiped clean after each measurement (Steenburgh et al. 2014b,a).

2) RADAR

Simulated LeS storm morphology is evaluated by comparison against NOAA NEXRAD Level-2 data (NOAA/NWS Radar Operations Center 1991) from Marquette, Michigan (KMQT), and Montague, New York (KTYX). We use observed equivalent radar reflectivity factor Z_e from the lowest elevation angle scans (0.5°) to compare with WRF-simulated reflectivity, calculated within the Thompson microphysics scheme. Before analysis, the radar data were interpolated to a 1 km × 1 km Cartesian grid. These data are most useful in close vicinity (50–100 km) of the radar as echoes associated with LeS storms may be as shallow as 1–2 km, allowing the radar beam to completely or partially overshoot the storm (Brown et al. 2007). We mostly focus on comparing spatial structures between simulated and observed Z_e, as uncertainties associated with overshooting and assumptions in microphysical properties used to calculate Z_e within WRF add uncertainty to comparisons of Z_e magnitude. However, limitations of radar observations are less severe for Case 2, where a LLAP band with 2–3-km-deep echoes was persistently positioned close to the location of KTYX (Minder et al. 2015; Campbell et al. 2016). For this case, we estimate storm-total P from the radar data using a Z–S relationship that is supported by manual observations, as in Minder et al. (2015) and Campbell et al. (2016). Compared to OWLeS manual observations of P, the radar estimate performs very well near the eastern shore of Lake Ontario, but underestimates by 23% over the Tug Hill Plateau (Minder et al. 2015; Campbell et al. 2016).

3) GLEN STATION DATA

For Case 1, we compare the simulations with observations collected atop offshore lighthouses and a small island as part of the Great Lakes Evaporation Network [GLEN; https://superiorwatersheds.org/GLEN/data.htm; Spence et al. (2019)]. Data collected include measurements of: air temperature, wind speed and direction, and relative humidity, as well as friction velocity and sensible heat and latent heat fluxes, calculated using eddy covariance techniques (Blanken et al. 2011). We focus on data from Stannard Rock Lighthouse, located in south-central Lake Superior. It is built upon an underwater reef with the nearest land more than 40 km away. We also consider data collected from Granite Island (Lake Superior), White Shoal (Lake Michigan), and Spectacle Reef (Lake Huron). For the flux data, measurement heights above mean lake level vary from about 27.2 (Granite Island) to 42.8 m (White Shoal). When comparing with WRF output we average all horizontal grid points within 0.02° latitude and longitude of the measurement location. Surface values are used for simulated turbulent fluxes (F_H, F_Q, u_*) and data from the second-lowest WRF Model grid cell (centered at 28 m AGL) are used for mean state variables (temperature, humidity, etc.) in order to roughly match the GLEN measurement heights.

3. Case study 1: Lake Superior, 10–13 February 2016

a. Event overview

Case 1 is a LeS event that produced snowfall on the Upper Peninsula of Michigan from 10 to 13 February 2016, associated with a prolonged period of northerly to northwesterly flow that transported cold air over Lake Superior. The synoptic setup for the event included a pair of troughs that approached from the northwest and passed over the Great Lakes region. As an example of the lower-tropospheric synoptic configuration, Fig. 2a shows 850-hPa heights, winds, and temperatures from the outermost domain of the control WRF simulation at 2100 UTC 12 February. At this time 850-hPa temperatures over Lake Superior ranged from about −30° to −22°C. Over the lake, temperatures at 850 hPa were persistently less than −20°C throughout the event. With lake surface temperatures of about 4°C (Fig. 1a) the surface to 850-hPa temperature difference ranged from about 24° to 34°C. This is indicative of strong overlake convective instability and well above the 13°C threshold used by forecasters as an indicator of significant LeS potential (e.g., Niziol et al. 1995). Additionally, lake ice coverage was limited to small areas in the immediate vicinity of the northern shores and isolated bays of Lakes Superior, Michigan, and Huron (e.g., Fig. 1a), allowing for large fetches of open water for lake–air fluxes to drive LeS.

The lake-effect convective clouds produced by this instability are evident in satellite imagery (e.g., Fig. 2b). They are organized into numerous horizontal convective rolls, as are typical when the winds are directed across the shorter axis of a lake (e.g., Kristovich 1993; Niziol et al. 1995). These have a width of about 5–10 km and are generally oriented parallel to the 850-hPa wind

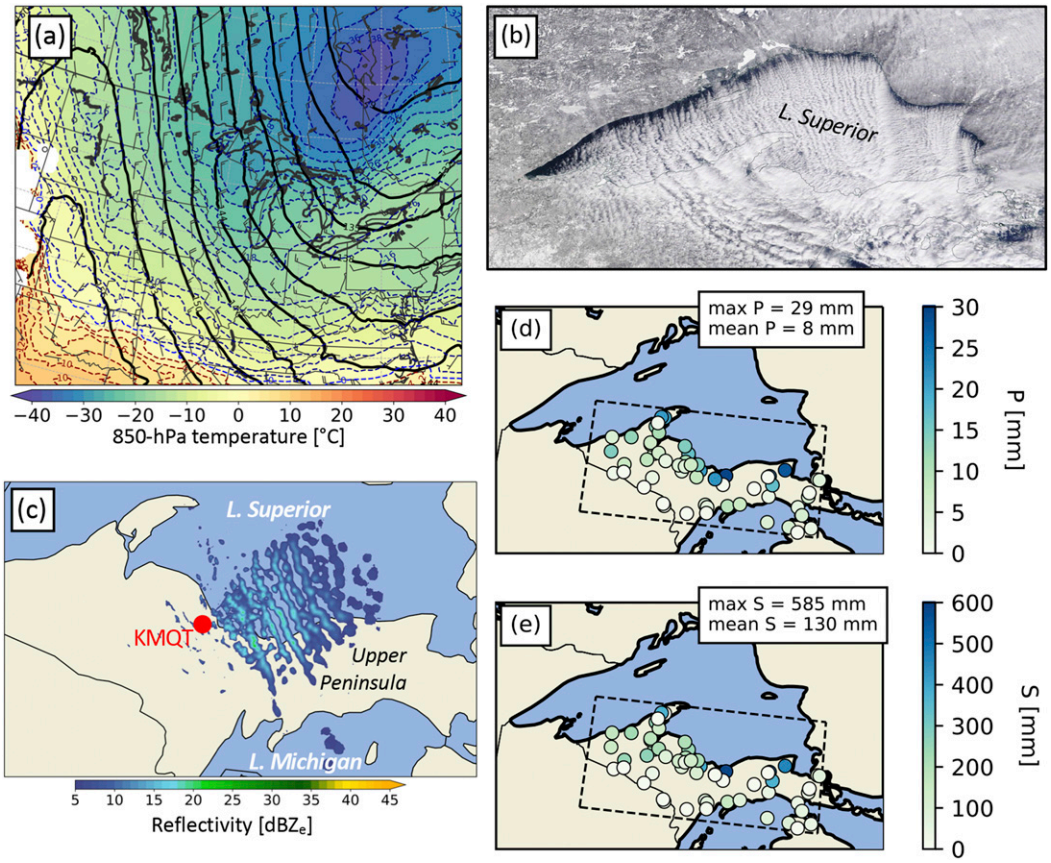

FIG. 2. Overview of Case 1: 10–13 Feb 2016. (a) Map of simulated 850-hPa temperatures (shaded), heights (contoured), and winds (full barb every 5 m s^{-1}) at 2100 UTC 12 Feb from WRF domain 1. (b) MODIS *Terra* "true color" imagery from about 1700 UTC 12 Feb. (c) Equivalent radar reflectivity factor (shaded) from the KMQT NEXRAD radar (red circle) at 2058 UTC 12 Feb. (d),(e) Accumulated *P* and *S* over the Upper Peninsula of MI from 10 to 13 Feb from GHCN stations (shaded circles), with maximum and mean values given in the inset box.

direction. This organization is also apparent in radar imagery from the KMQT radar on the Upper Peninsula (e.g., Fig. 2c), which depicts narrow bands of reflectivity associated with the snowfall produced by these clouds. However, their structure is only well depicted at close range (roughly ≤75 km) as the radar beam overshoots the shallow convection at larger ranges.

Event-total snowfall measured over the Upper Peninsula shows accumulated *P* as high as 29 mm and *S* as high as 585 mm, with the largest accumulations measured near the coast (Figs. 2d,e). There is large spatial variability in accumulations, with nearby stations recording drastically different amounts of snowfall. This is likely in part due to the precise positioning of narrow snowbands and in part due to spatial variability in wind-induced gauge undercatch.

b. *Simulated convection and snowfall*

As an example of the simulated storm morphology and intensity, Fig. 3 shows the WRF-simulated equivalent radar reflectivity factor (dBZ_e) in the vicinity of the KMQT radar at 2100 UTC 12 February. All simulations show echoes associated with lake-effect convection that forms over Lake Superior and is advected south over the Upper Peninsula, reaching the northern end of Lake Michigan. Note, the boundary layer circulations associated with this convection are only marginally resolved by the 1.33-km grid and the partially explicit representation of these motions likely violates some of the assumptions underlying the PBL schemes used (Ching et al. 2014). Nevertheless, a majority of the simulations produce narrow wind-parallel bands that are broadly consistent with the KMQT radar observations in close vicinity of the radar, where beam overshooting should be modest. These simulations vary in their band morphologies, with some producing more linear bands (YSU_MM5, BOLA_MM5, GBM_MM5) while others produce linear bands that evolve into more cellular structures in the downwind direction (MYNN, MYJ, SH_MM5, MYNN_MM5). The QNSE and TEMF

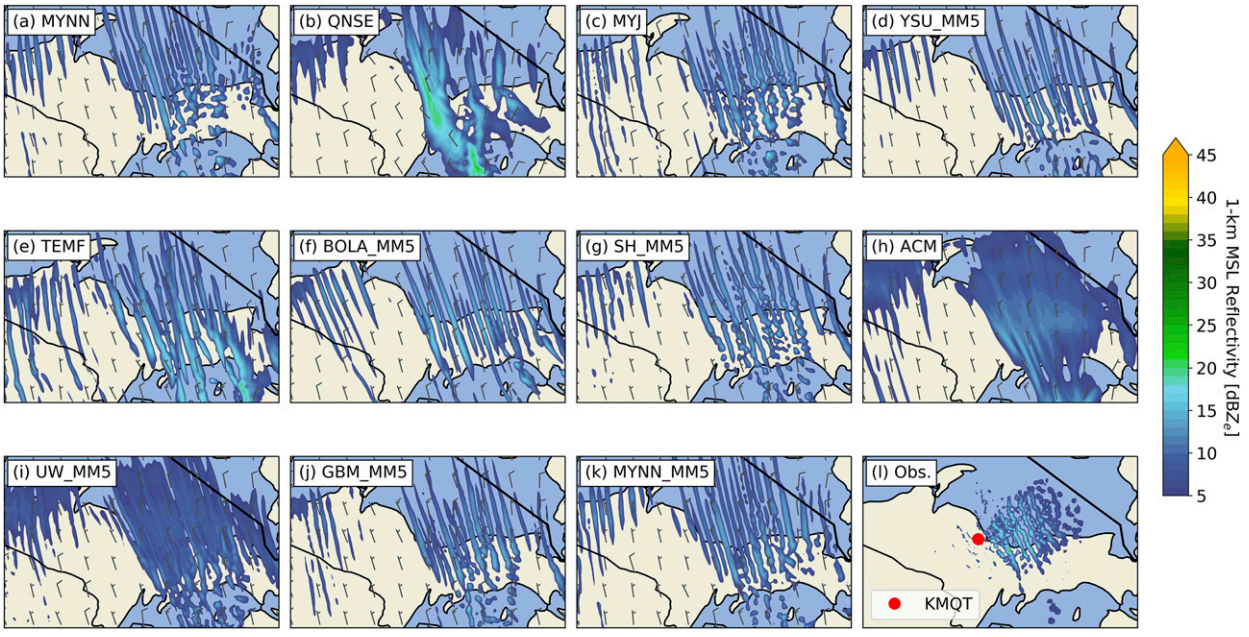

FIG. 3. Comparison of WRF-simulated and observed equivalent radar reflectivity factor dBZ_e at 2100 UTC 12 Feb 2016. (a)–(k) WRF-simulated dBZ_e at 1 km MSL (shading) and 10-m winds (full barb every 5 m s^{-1}). (l) KMQT NEXRAD radar-observed dBZ_e, as in Fig. 2c.

experiments also produce wind-parallel bands, but the bands are less numerous, broader in horizontal scale, and have higher dBZ_e. The ACM and UW_MM5 experiments produce some banded features, but the simulated morphologies are dominated by a broad region of relatively uniform reflectivity characteristic of stratiform clouds. These differences in storm morphology are at least partially attributable to the PBL scheme used, as schemes using an identical SL scheme (revised MM5) show diverse morphologies. The differences in storm morphologies seen in Fig. 3 are broadly representative of the differences found throughout the duration of the event (not shown).

The consequences of these differences in storm morphology and intensity are apparent when examining the event-total P (Fig. 4). Over the Upper Peninsula, the experiments with narrow linear bands produce spatially averaged P accumulations of 9.1–10.3 mm, with most showing substantial small-scale spatial variability. The experiments with broader and more intense bands (QNSE, TEMF) produce larger accumulations, around 11.4–11.7 mm, and also exhibit large spatial variations. The experiments with broad stratiform morphologies (ACM, UW_MM5) vary in their average accumulations from 9.6 to 14.4 mm, but exhibit less spatial variability. Uncertainties in the snowfall observations make it difficult to draw firm conclusions about the relative accuracy of the simulations. However, the observations (Fig. 2d) appear to be most consistent with the simulations with smaller, but spatially variable, P accumulations.

c. *Simulated fluxes*

As discussed above, there are several differences in how the SL schemes parameterize the fluxes of sensible and latent heat over water. As these fluxes are a fundamental forcing of LeS, we compare the simulated lake-averaged fluxes. Figure 5 shows the event-averaged F_H. For the MYNN control simulation, averaged over Lake Superior, $F_H = 290\ \mathrm{W\,m^{-2}}$, toward the upper end of the range of values that have been measured during LeS events. Locally, F_H reaches as high as $443\ \mathrm{W\,m^{-2}}$, with the largest fluxes located near the northern shores of the lake, where the cold continental air first encounters the warm waters of the lake.

There is substantial variation in simulated F_H between schemes. Several experiments simulate F_H within $10\ \mathrm{W\,m^{-2}}$ of the MYNN control (YSU_MM5, SH_MM5, UW_MM5, GBM_MM5). One experiment, BOLA_MM5, simulates lake-average F_H fluxes $35\ \mathrm{W\,m^{-2}}$ lower than MYNN. Several experiments simulate moderately higher lake-average F_H fluxes, exceeding MYNN by 13–26 $\mathrm{W\,m^{-2}}$ (MYJ, TEMF, MYNN_MM5). Two experiments (QNSE and ACM) stand out as outliers with extremely high fluxes, exceeding MYNN by 154 and $90\ \mathrm{W\,m^{-2}}$.

Simulated F_Q also varies considerably between schemes (Fig. 6). For MYNN, lake-average $F_Q = 146\ \mathrm{W\,m^{-2}}$, which is substantially smaller than F_H and toward the middle of

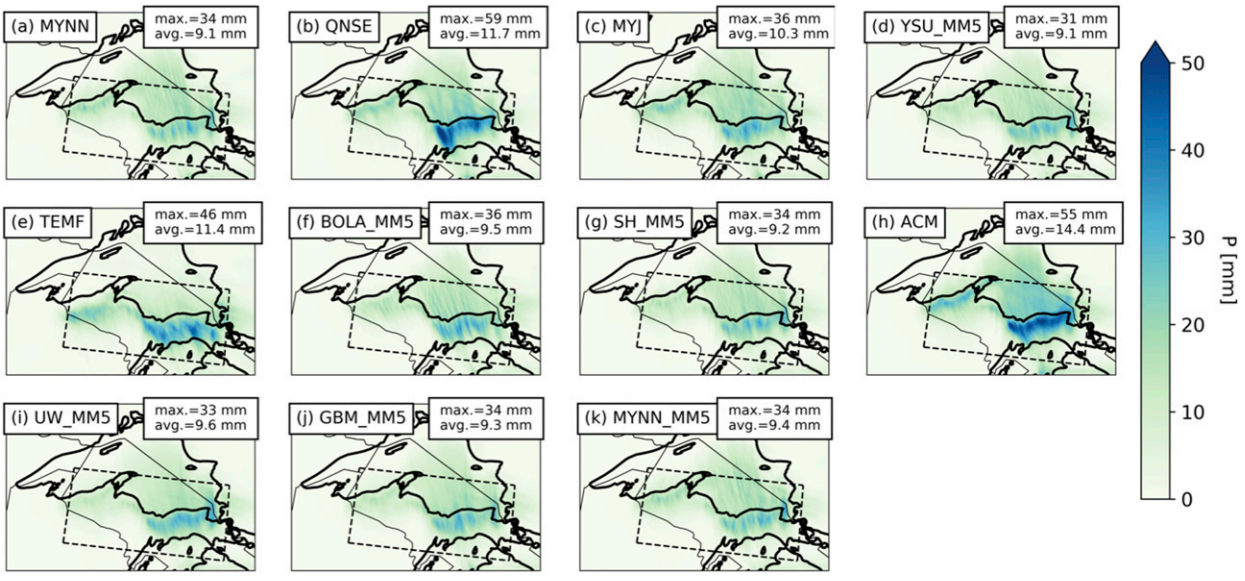

FIG. 4. (a)–(k) WRF-simulated accumulated P for 0600 UTC 10 Feb–0000 UTC 14 Feb 2016. Average and maximum values over the Upper Peninsula of Michigan (overland region within dashed box) are noted in the inset boxes.

the range of previously observed values. The flux F_Q varies across experiments, but not as substantially as F_H. Most schemes simulate lake-average F_Q values that differ from MYNN by no more than $10\,\mathrm{W\,m^{-2}}$. Several schemes simulate higher fluxes, with ACM being the most extreme outlier, with lake-average $F_Q = 58\,\mathrm{W\,m^{-2}}$ higher than in MYNN.

Surface momentum fluxes, as quantified by u_*, also vary, though the relative magnitudes between schemes are not closely related to the magnitude of the heat and moisture fluxes (Fig. 7). For u_*, MYNN simulates the highest fluxes with a lake-average value of $0.47\,\mathrm{m\,s^{-1}}$.The other experiments simulate lake-average u_* values that are 0.02–$0.12\,\mathrm{m\,s^{-1}}$ lower.

The above-described variations in simulated surface fluxes appear to have important impacts on the simulated convection and snowfall. Experiments with high heat and moisture fluxes (QNSE, TEMF, ACM) produce

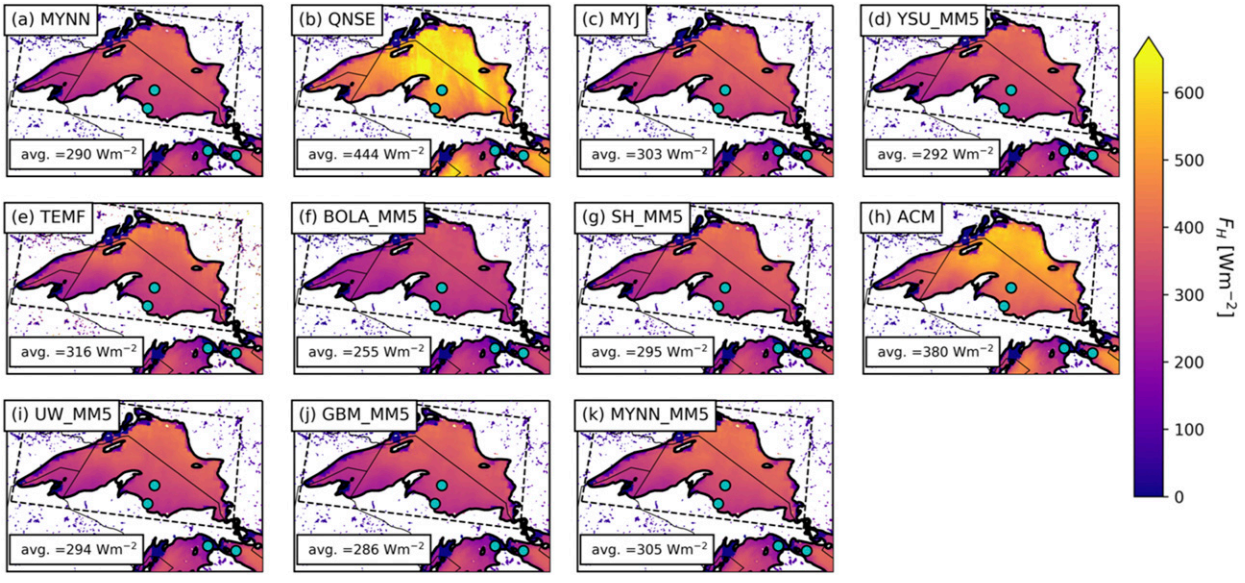

FIG. 5. (a)–(k) WRF-simulated average F_H for 0600 UTC 10 Feb–0000 UTC 14 Feb 2016. Average values over Lake Superior are noted in inset boxes. Sites of GLEN stations, labeled in Fig. 1a, are marked with cyan circles.

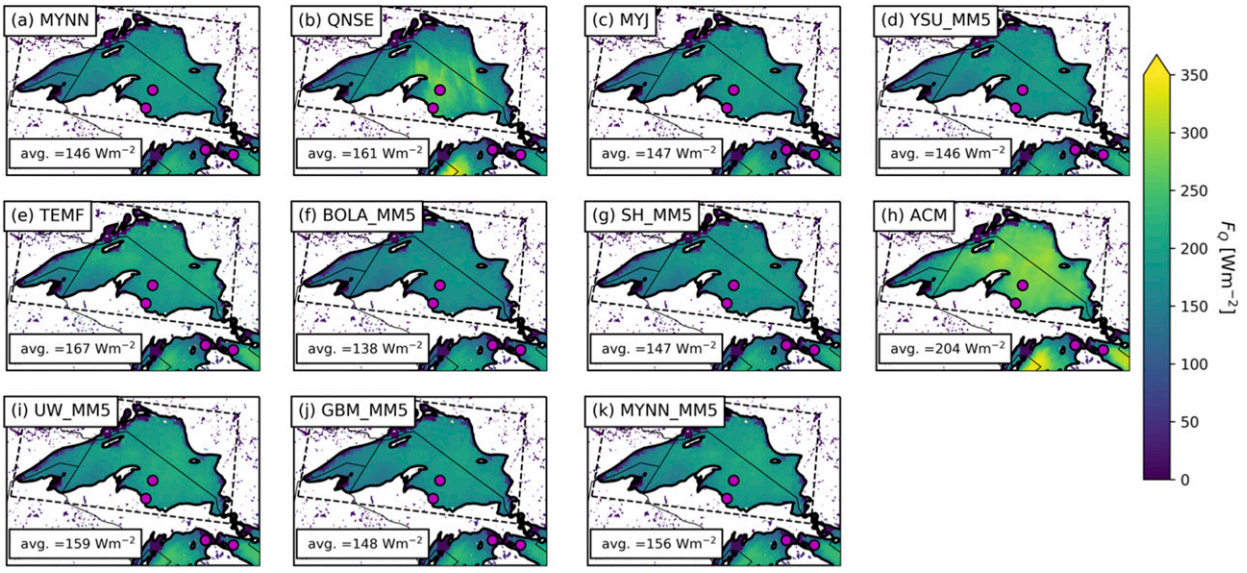

FIG. 6. (a)–(k) WRF-simulated average F_Q for 0600 UTC 10 Feb–0000 UTC 14 Feb 2016. Average values over Lake Superior are noted in inset boxes. Sites of GLEN stations, labeled in Fig. 1a, are marked with magenta circles.

more intense convection (Fig. 3) and larger snowfall totals (Fig. 4). Larger surface fluxes in QNSE and TEMF may also help to explain some of the band morphology differences, as larger fluxes lead to deeper boundary layer depths (not shown), which have been associated with longer wavelengths of horizontal convective roll circulations (e.g., Weckwerth et al. 1997).

To further explore the connection between fluxes and snowfall, in Fig. 8 we compare F_H and F_Q, averaged over the duration of the event and the surface of Lake Superior, with the event-total P, averaged over the Upper Peninsula. P is correlated with the total flux, $F_H + F_Q$ ($r = 0.74$, $p < 0.01$) and the relationship shows some interesting groupings. Most experiments, including MYNN, plot toward the lower-left corner, with P around 8 mm and $F_H + F_Q$ around 445 W m^{-2}. The experiments using the revised MM5 SL scheme produce very similar P and, with the exception of BOLA_MM5,

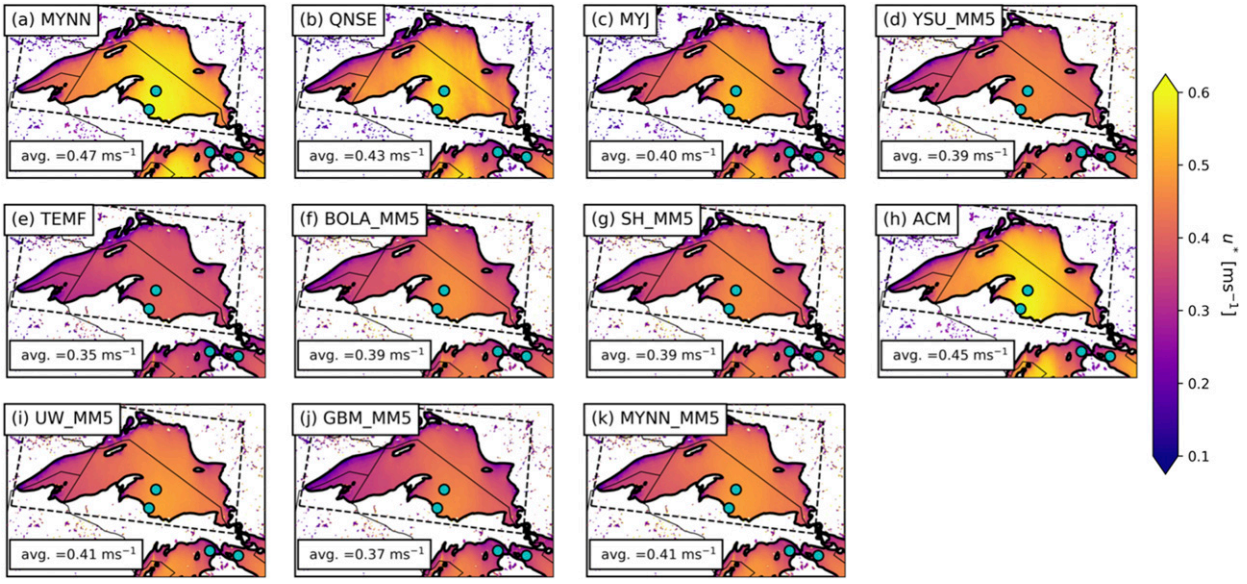

FIG. 7. (a)–(k) WRF-simulated average u_* for 0600 UTC 10 Feb–0000 UTC 14 Feb 2016. Average values over Lake Superior are noted in inset boxes. Sites of GLEN stations, labeled in Fig. 1a, are marked with cyan circles.

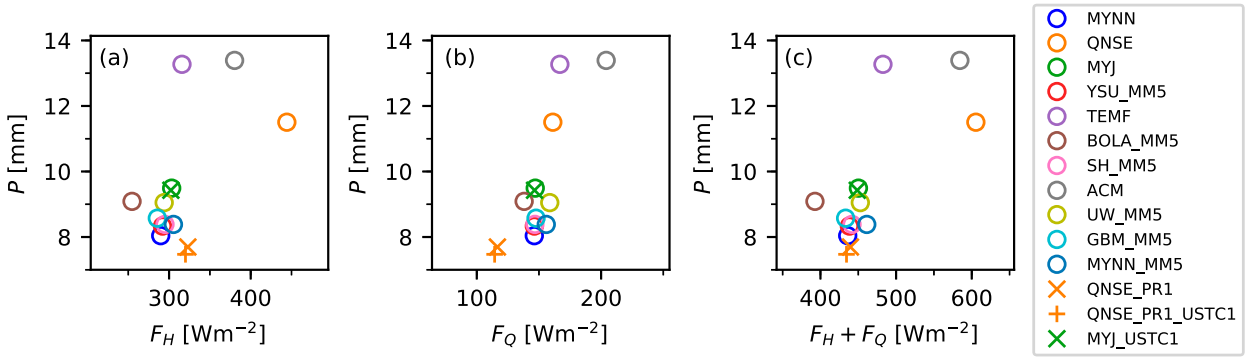

FIG. 8. (a)–(c) Comparison of event-average fluxes (F_H, F_Q) against event-total P for 0600 UTC 10 Feb–0000 UTC 14 Feb 2016. Fluxes are averaged over the surface of Lake Superior, as in Figs. 5 and 6; P is averaged over the Upper Peninsula of MI, as in Fig. 4. Open circles show results from multischeme experiment suite summarized in Table 1. Other symbols show results from QNSE and MYJ parameter sensitivity experiments summarized in Table 2.

very similar fluxes. The remaining experiments (QNSE, TEMF, ACM) produce substantially higher fluxes and snowfall, and do not exhibit a clear clustering.

From this analysis, it is not straightforward to determine which experiments are most physically realistic. Comparison with gauge measurements suggest that the high-P schemes produce excessive snowfall (Fig. 4), however, observational uncertainties, including potential gauge undercatch, prevent drawing firm conclusions. We next turn to direct measurements of lake–atmosphere fluxes to evaluate the physical realism of the simulations.

d. Comparison with GLEN observations

First, we compare the time evolution of standard meteorological variables measured at Stannard Rock with those simulated by the various experiments over the duration of the event (Figs. 9a–d). Observations show air temperatures from around −10° to −15°C, northerly winds around 10–15 m s^{-1}, and specific humidity around 1–1.5 g kg^{-1}. The lowest air temperatures, largest instability (as measured by lake–air temperature difference), and strongest winds are found from about 1200 UTC 12 February–1200 UTC 13 February.

The simulations generally capture the overall conditions and evolution of the event. Closer inspection reveals some difference between experiments and biases relative to observations. TEMF and QNSE predict generally higher air temperatures than the other experiments, and are often 1°–2°C higher than observations. Wind speeds are biased low in all experiments throughout most of the event. Mixing ratios are generally well simulated, but TEMF is biased substantially too moist.

Large values of F_H are measured throughout the event, ranging from 158 to 547 W m^{-2}, with the largest fluxes coinciding with the strongest instability after 1200 UTC 12 February (Fig. 9e). Large values of F_Q are also measured, ranging from 116 to 271 W m^{-2}, though they do not reach as high or show as much temporal variability as F_H (Fig. 9f). For both F_H and F_Q, some data are missing on 12–13 February. Measurements of u_* show more high-frequency variability than the model output, with values ranging from 0.17 to 0.89 m s^{-1} and the most consistently enhanced values during 1200 UTC 12 February–1200 UTC 13 February when wind speed and instability were both high (Fig. 9g).

Most of the simulations perform well at reproducing the observed F_H and F_Q, with differences of around 40 W m^{-2} relative to observations and a modest positive bias for F_H (Figs. 9e,f). The exceptions are the QNSE and ACM experiments, which produce much larger fluxes than observed, especially during the period of largest instability on 12–13 February. ACM shows a relatively consistent positive bias of around 100 W m^{-2} for F_H and F_Q. For much of the event, QNSE shows a similar bias to ACM for F_H and minimal bias for F_Q. However, abrupt jumps of about 250–500 W m^{-2} are found in the QNSE simulated F_H and F_Q. These lead to very large transient biases, at times exceeding 800 W m^{-2} for F_H. Due to the large high-frequency variability in the observations, the comparison with observed u_* is less definitive (Fig. 9g). At most times the simulated values span a range of about 0.25 m s^{-1}. The simulated values do not exhibit the same high-frequency variations as the measurements and often bracket the observed variability. The largest u_* is simulated by QNSE, ACM, and MYNN, while the smallest is simulated by TEMF.

Figure 9g also provides insight into the cause of the abrupt jumps in F_H and F_Q simulated by QNSE. The thin horizontal dashed lines show the thresholds used in QNSE and MYJ to delineate between different regimes for the calculation of roughness lengths [see discussion

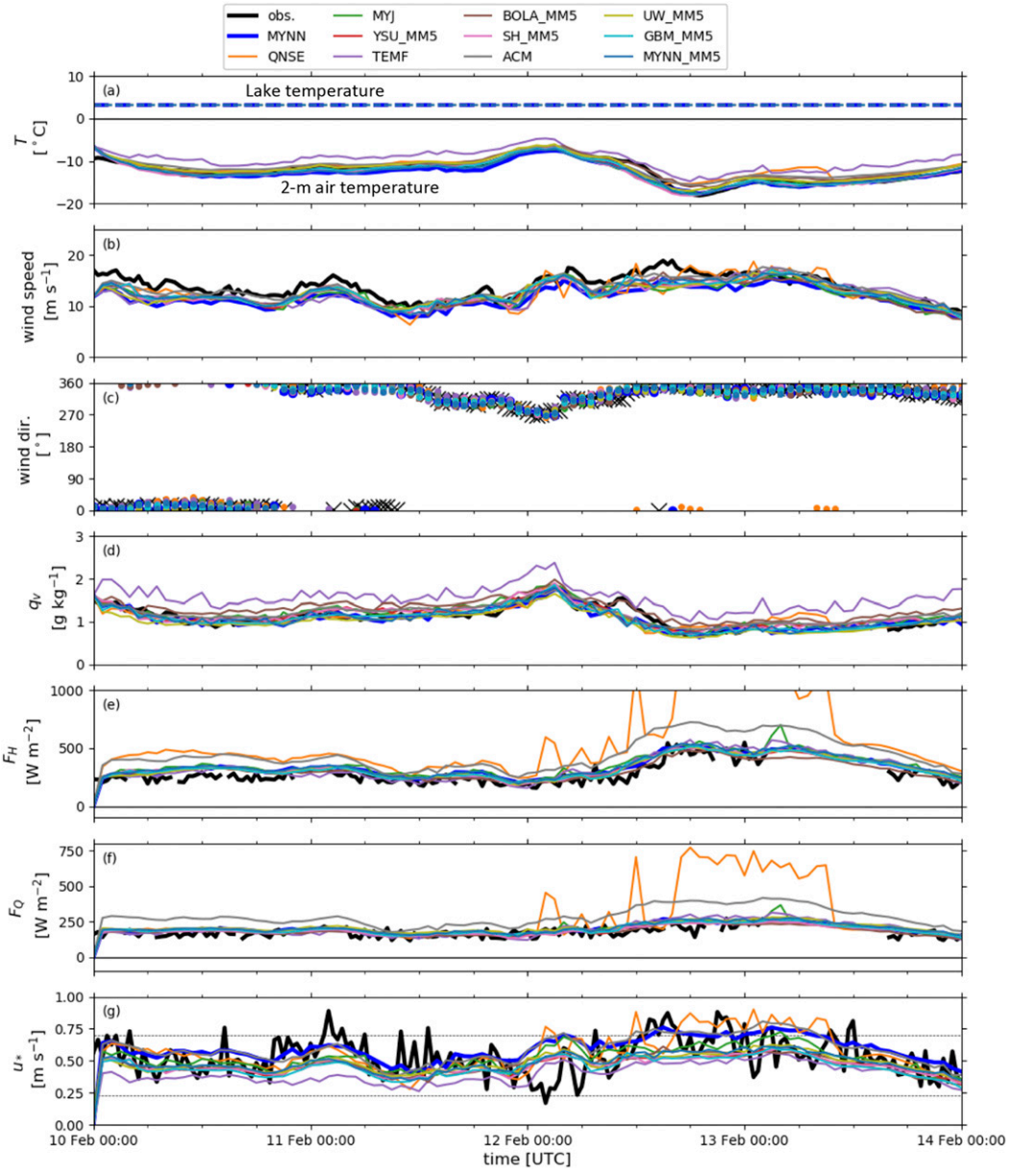

FIG. 9. Comparison of WRF-simulated and observed near-surface conditions at the Stannard Rock GLEN station: (a) air temperature (solid) and lake surface temperature (dashed), (b) wind speed, (c) wind direction, (d) water vapor mixing ratio, (e) F_H, (f) F_Q, and (g) u_*. WRF results are the spatial averages of all grid points within 0.02° latitude and longitude of the station. For (a)–(d) simulated values from the second-lowest WRF Model level (about 28 m AGL) are used. For (e) and (f) simulated surface fluxes are used. Dotted gray lines in (g) show threshold values of u_* used to determine regimes for roughness calculations in QNSE and MYJ [see section 2a(2)].

in section 2a(2)]. In QNSE, when u_* crosses the threshold of 0.7 m s^{-1}, above which $z_{o,h}$ and $z_{o,q}$ are set equal to z_o, large upward jumps in F_H and F_Q occur. Despite a similar roughness formulation, only one such jump is found for MYJ as the threshold is is only briefly crossed, on 13 February, in that experiment.

One limitation of the above analysis is that it only considers a single point location. To expand our analysis we also compare with observations from Granite Island, Spectacle Reef, and White Shoal in Fig. 10, limiting this additional analysis to F_H for brevity. The heat fluxes observed at Granite Island and Spectacle Reef are similar to those at Stannard Rock. There are some differences in the time evolution at Spectacle Reef, which is located on Lake Huron, experiences different upwind overwater fetch as a function of wind direction than

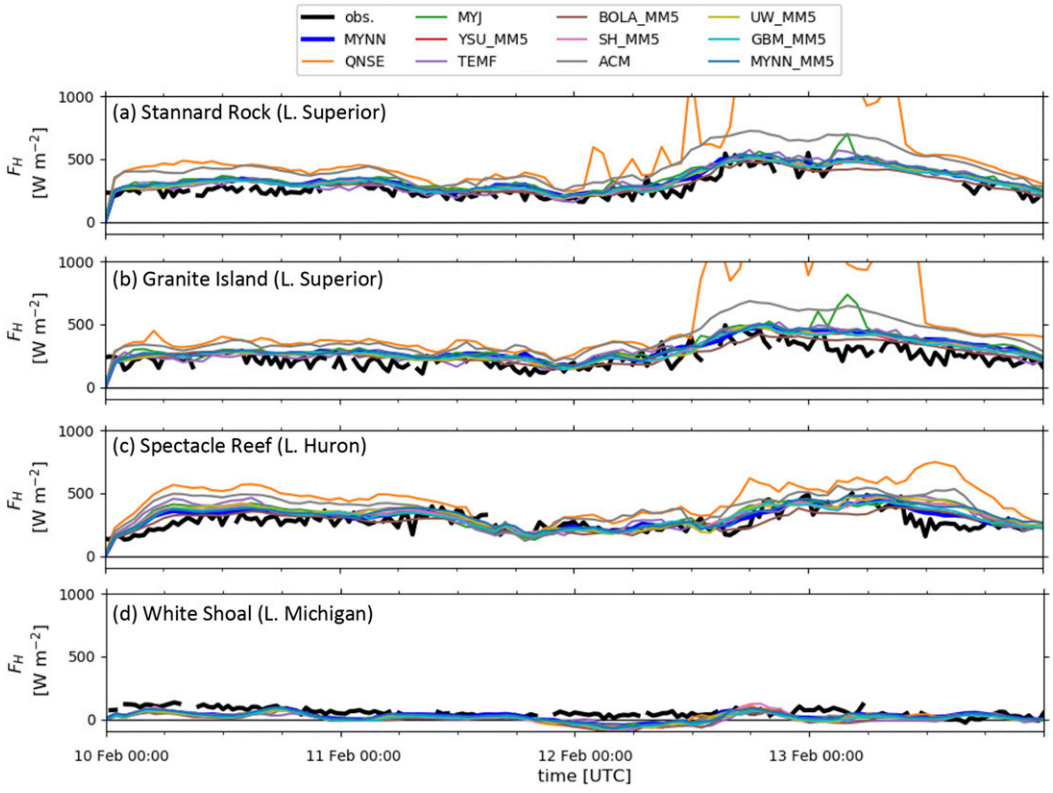

FIG. 10. Comparison of WRF-simulated and observed F_H, as in Fig. 9e, but at various GLEN stations: (a) Stannard Rock, (b) Granite Island, (c) Spectacle Reef, and (d) White Shoal.

Stannard Rock, and, due to its location to the southeast, may experience changes in synoptic conditions with a delay of several hours relative to Stannard Rock. Fluxes at White Shoal are greatly subdued, likely due to the presence of near complete lake ice coverage between the site and the northern shore of Lake Michigan throughout the event (other GLEN sites considered had upwind fetches dominated by open water).

The simulations generally capture the variability of F_H between sites. The differences in timing of fluxes at Spectacle Reef are well simulated. The reduced fluxes at White Shoal are also captured, though the simulations show a period of weak negative (downward) fluxes on 12 February that are not seen in the observations. At Granite Island and Spectacle Reef, the differences between experiments are generally consistent with those discussed above: most experiments are clustered near or slightly above the observations, while ACM and QNSE produce a large positive bias in fluxes, especially during periods of large observed F_H. At Granite Island, QNSE again shows large jumps in F_H associated with periods of simulated $u_* > 0.7\,\mathrm{m\,s^{-1}}$ (not shown). MYJ shows some similar behavior, although briefer and less pronounced. No such jumps are found for MYJ and QNSE at Spectacle Reef, as the u_* threshold is not exceeded.

Based on this comparison, the large fluxes predicted by ACM and QNSE (and to a lesser extent TEMF) appear to be unrealistic. These biases likely lead to an unrealistic moistening and destabilizing of the boundary layer, artificially enhancing lake-effect convection and snowfall.

4. Case study 2: Lake Ontario, 11 December 2013

a. *Event overview*

Case 2 occurred from 0000 UTC 11 December to 0000 UTC 12 December 2013 during the OWLeS field campaign and has been the subject of numerous studies. It was associated with a broad upper-level trough and zonal flow with 850-hPa temperatures around −15°C (Campbell et al. 2016) and lake temperatures exceeding 6°C (Fig. 1). The along-lake flow and strong instability supported the formation of land-breeze fronts that helped to organize an intense, 2–4-km-deep, long-lake-axis-parallel band of convection that extended to the east of Lake Ontario (Minder et al. 2015; Welsh et al. 2016; Campbell and Steenburgh 2017; Steenburgh and Campbell 2017; Bergmaier et al. 2017). Figure 11a shows an example of band morphology from radar reflectivity observed from the KTYX radar at 0900 UTC.

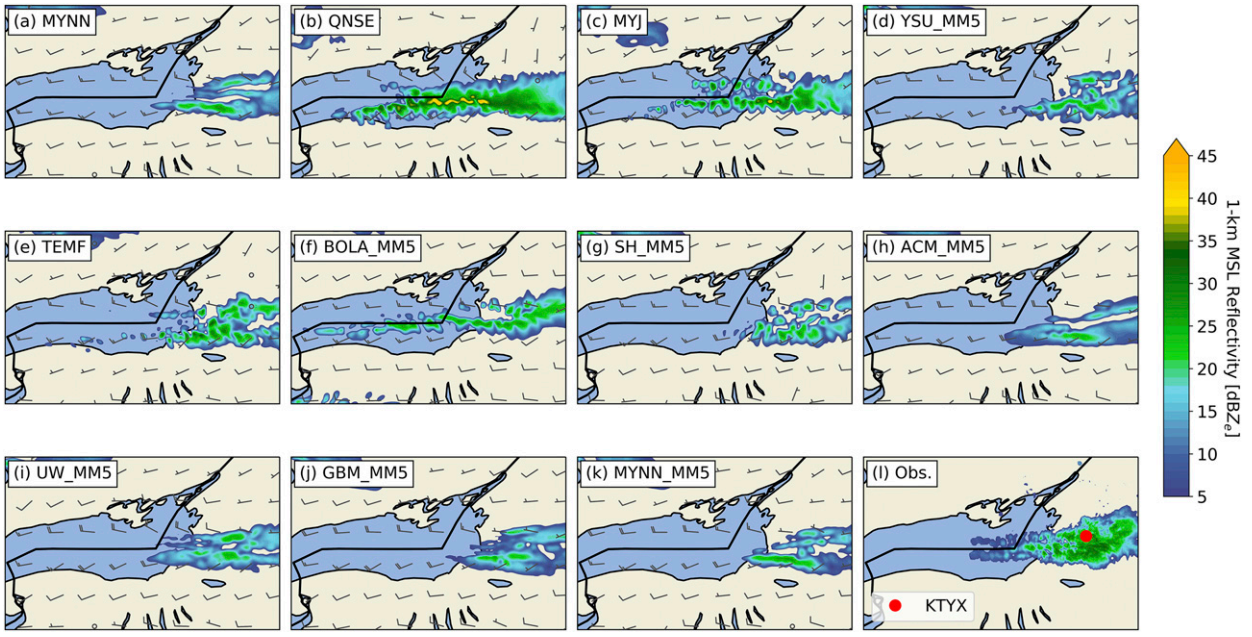

FIG. 11. Comparison of WRF-simulated and observed equivalent radar reflectivity factor dBZ_e at 0900 UTC 11 Dec 2013. (a)–(k) WRF-simulated dBZ_e at 1 km MSL (shading) and 10-m winds (barbs). (l) KTYX NEXRAD radar-observed dBZ_e, as in Fig. 2c.

The band was relatively stationary, centered on the Tug Hill Plateau during most of the event, with some variations in band position and organization, related in part to the passage of shortwave troughs (Campbell et al. 2016).

Intense snowfall occurred within this band. Manual observations recorded 24-h accumulated $S = 102.5$ cm and $P = 6.4$ cm over the Tug Hill Plateau, and smaller accumulations ($S = 47.8$ cm, $P = 3.4$ cm) nearer to the coast (Minder et al. 2015). Radar-estimated storm-total P (Fig. 12a) shows a zonally oriented band of snowfall with an inland maximum caused by orographic uplift and land-breeze frontal forcing (Minder et al. 2015; Campbell and Steenburgh 2017).

b. Simulated convection and snowfall

An example of simulated storm morphology and intensity is shown in Fig. 11. All simulations produce a zonally oriented band in a similar position to what is

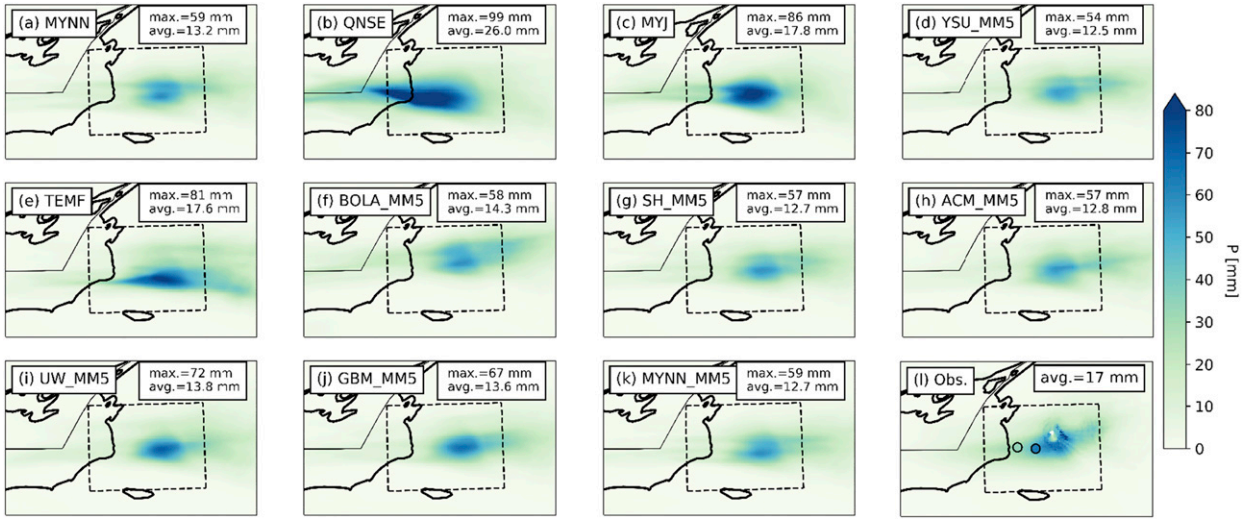

FIG. 12. Comparison of WRF-simulated and observed accumulated P for 11 Dec 2013. (a)–(k) WRF-simulated P. (l) P measured by OWLeS manual observations (filled circles) and estimated by KTYX radar (shading). Average and maximum values over the Tug Hill Plateau region (overland region within dashed box) are noted in the inset boxes.

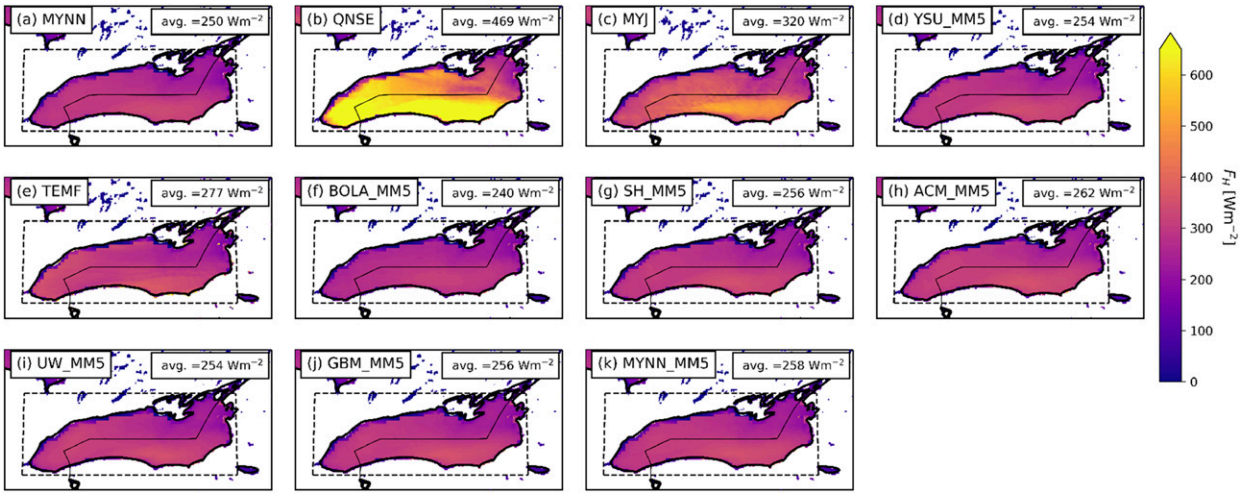

FIG. 13. (a)–(k) WRF-simulated average F_H for 11 Dec 2013. Average values over Lake Ontario are noted in the inset boxes.

observed. However, the simulated bands vary in their structure and intensity. Some produce strong organization into single bands (QNSE, BOLA_MM5) or multiple bands (MYNN, ACM, UW_MM5), whereas others produce less organized and more cellular bands (MYJ, TEMF, SH_MM5). It is difficult to determine which morphology is most realistic, especially considering that the morphology evolved substantially throughout the event (Campbell et al. 2016). Between the eastern shore of Lake Ontario and the KTYX radar, where beam overshooting should be modest, most simulations produce reflectivity consistent with observations, though QNSE appears to produce overly intense convection, with reflectivity well in excess of 40 dBZ_e. The simulations with more-intense bands (QNSE, MYJ, TEMF) also appear to exhibit stronger meridional convergence of the low-level winds, suggestive of a stronger land-breeze response to enhanced fluxes and/or strong secondary circulations induced by enhanced convection (e.g., Bergmaier et al. 2017).

Snowfall amounts downwind of Lake Ontario show large variations across the simulations (Fig. 12). Simulated storm-total P, averaged over the dashed region in Fig. 12, varies from 12.5 to 26.0 mm as compared to the radar estimate of 17 mm. Most simulations are biased somewhat low in this metric, whereas QNSE is biased substantially high. Similarly, most simulations appear biased low in terms of maximum P, while QNSE, MYJ, and TEMF appear biased high. Caution is warranted in comparing the simulations with radar-estimated P, which has substantial uncertainties, though comparing with manual point measurements from OWLeS (shaded circles in Fig. 12) indicates similar biases. The simulations mostly agree with radar and manual observations in terms of the spatial distribution of snowfall, showing a maximum downwind of the shoreline. However, QNSE appears to produce an unrealistic upwind shift in the western boundary of the region of heavy snowfall.

c. *Simulated fluxes*

For Case 2, as in Case 1, simulated lake–atmosphere fluxes are strong and vary substantially between experiments. Figure 13 shows the event-averaged simulated F_H. Lake-average F_H ranges from 240 to 469 W m^{-2}. Large variations are also found in lake-average F_Q, which ranges from 236 to 429 W m^{-2} (not shown).

Again, variations in simulated fluxes appear to strongly impact snowfall (Fig. 14). Comparing lake-average $F_H + F_Q$ with downwind storm-total P (Fig. 14c) reveals a strong correlation ($r = 0.92$, $p < 0.01$). A majority of simulations are clustered together, with total fluxes from about 450 to 550 W m^{-2} and accumulated P from about 13 to 15 mm. Three outliers have much higher fluxes and snowfall (QNSE, TEMF, and MYJ). These results are largely consistent with those from Case 1 (Fig. 8), with the primary difference being the position of MYJ, which shows relatively larger fluxes and snowfall in this case. The larger fluxes in MYJ are associated with a higher u_* in Case 2 which exceeds the 0.7 m s^{-1} threshold in the MYJ SL scheme, causing a drastic increase in MYJ-simulated fluxes as occurs in QNSE (not shown).

Observations of lake–atmosphere fluxes are not available for Case 2, so we cannot directly evaluate the realism of the simulated fluxes. However, the similarity of the results with those of Case 1 suggest that the high-flux schemes, which were shown to have excessive fluxes relative to the GLEN observations, are likely biased in this case as well. This is supported by the above comparison with radar-estimated snowfall,

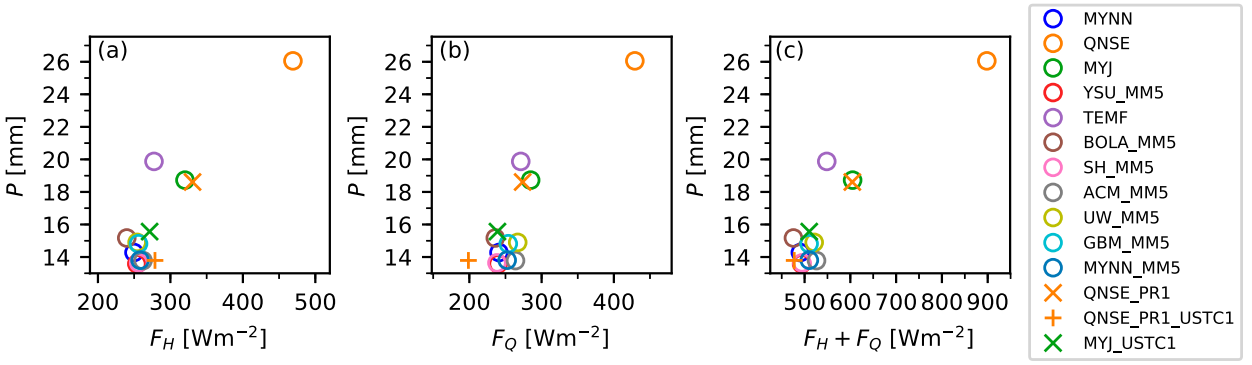

FIG. 14. (a)–(c) Comparison of event-average fluxes (F_H, F_Q) against event-total P for 11 Dec 2013. Fluxes are averaged over the surface of Lake Ontario, as in Fig. 13; P is averaged over the Tug Hill Plateau region, as in Fig. 12. Open circles show results from multischeme experiment suite summarized in Table 1. Other symbols show results from QNSE and MYJ parameter sensitivity experiments summarized in Table 2.

which suggests that the high-flux schemes produce excessive snowfall maxima.

5. Parameter sensitivity experiments

To better isolate some of the causes of flux and snowfall differences between schemes we conduct controlled parameter sensitivity experiments wherein we vary parameters within the QNSE and MYJ schemes (Table 2). For QNSE we set $P_R = 1$ (QNSE_PR1), increasing it from the default value of 0.72 in order to make it consistent with most other schemes (Table 1). For MYJ we increase the critical u_* value for the "rough with spray" regime to 1.0 m s^{-1} (MYJ_USTC1), in an attempt to reduce the occurrence of unrealistic jumps in fluxes. We also change both of these parameters in an additional QNSE experiment (QNSE_PR1_USTC1). These new configurations are used to conduct additional simulations of Cases 1 and 2.

Lake-average results from these sensitivity experiments are shown with × and + symbols in Figs. 8 and 14. For Case 1, the most notable difference is found for the QNSE_PR1 experiment, where, relative to the QNSE experiment, P over the Upper Peninsula is reduced by 3.8 mm and overlake $F_H + F_Q$ is reduced by 166 W m^{-2} as a consequence of increasing P_R. This brings the values into much closer agreement with the cluster of lower-flux, lower-P schemes (Fig. 8). For this case, changes to the critical u_* value in the QNSE_PR1_USTC1 and MYJ_USTC1 experiments lead only to modest reductions in fluxes and P.

The temporal evolution of simulated fluxes from the Case 1 sensitivity experiments is shown, and compared to GLEN observations at Stannard Rock, in Fig. 15. The increase of P_R in QNSE_PR1 reduces the fluxes throughout the event relative to QNSE, with large reductions in F_H and F_Q that bring them into much better agreement with the observations. The abrupt transitions in F_H and F_Q found in QNSE are mostly eliminated, with the exception of a brief spike that occurs early on 13 February. This occurs because increases in P_R indirectly lead to reductions in u_*, likely via weaker PBL turbulence and downward momentum mixing, such that the critical u_* value is only briefly exceeded in QNSE_PR1. The time series of u_* also reveals why minimal changes are found when reducing the critical u_* in the QNSE_PR1_USTC1 and MYJ_USTC1 experiments: since u_* only briefly crosses the threshold in MYJ and QNSE_PR1, the impacts of this change on F_H and F_Q, while apparent, are confined to a short period of time.

For Case 2 (Fig. 14) increasing P_R in QNSE_PR1 again leads to large reductions in downwind P (by 7.4 mm) and

TABLE 2. As in Table 1, but for parameter sensitivity experiments. For each experiment, altered parameters are highlighted with bold text.

Experiment	PBL scheme	SL scheme	P_R	Roughness
QNSE_PR1	Quasi-normal scale elimination[a]	QNSE	**1**	From[b]
QNSE_PR1_USTC1	Quasi-normal scale elimination[a]	QNSE	**1**	From[b], **but critical $u_* = 1$ m s^{-1}**
MYJ_USTC1	Mellor–Yamada–Janjić[c]	MYJ	1	From[b], **but critical $u_* = 1$ m s^{-1}**

[a] Mellor and Yamada (1982), Janjić (2001), and Sukoriansky et al. (2005)
[b] Janjić (1994)
[c] Mellor and Yamada (1982) and Janjić (1994, 2001)

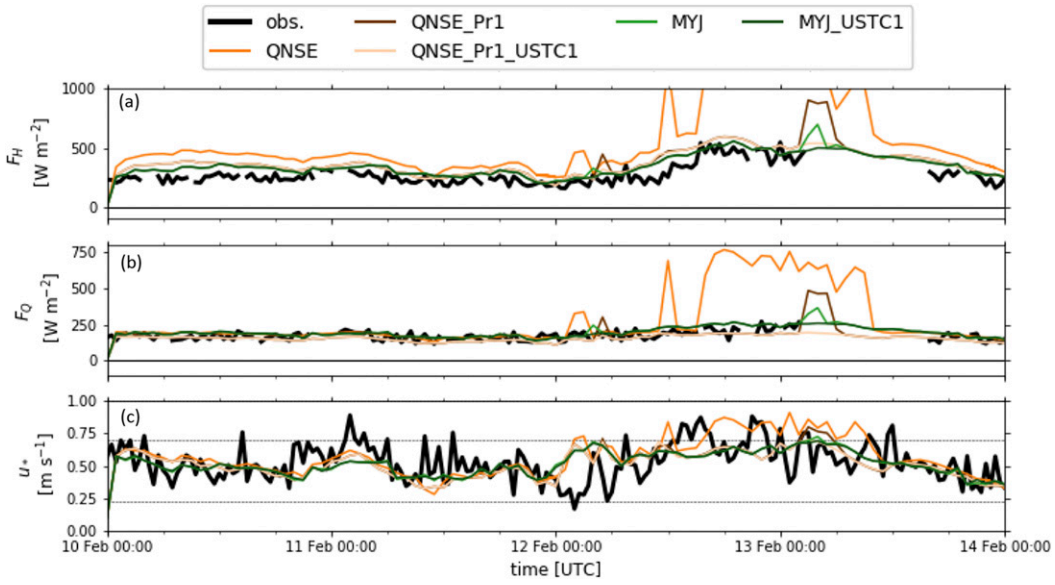

FIG. 15. Comparison of 10–13 Feb 2016 WRF-simulated fluxes from sensitivity experiments with observed fluxes at Stannard Rock GLEN station: (a) F_H, (b) F_Q, and (c) u_*.

overlake $F_H + F_Q$ (by 294 W m^{-2}). While these reductions bring the results into better agreement with the lower-flux lower-P simulations (Fig. 14) and the observed P (Fig. 12), QNSE_PR1 still shows notably higher P and fluxes. However, in Case 2, increasing the critical u_* value in QNSE_PR1_USTC1 has a substantial impact, further reducing downwind P (by 4.8 mm) and overlake $F_H + F_Q$ (by 127 W m^{-2}), bringing the results into better agreement. Increasing the critical u_* in MYJ_USTC1 leads to similar reductions in P and fluxes. The contrasting sensitivity to critical u_* in Cases 1 and 2 can be understood in terms of differences in the simulated momentum fluxes between the cases. For Case 2, u_* exceeds the critical value of 0.7 m s^{-1} over much of Lake Ontario for the majority of the event in QNSE, QNSE_PR1, and MYJ (not shown), such that changing the threshold value has a sustained, and cumulatively large, impact.

Taken together, the results of these parameter sensitivity experiments highlight the primary causes of the large fluxes and P simulated when using the QNSE and MYJ SL schemes and reveal that targeted parameter changes can bring their results into better agreement with other schemes and observations.

6. Discussion

Our results are broadly consistent with those of Conrick et al. (2015), who also documented strong sensitivity of simulated lake-effect snowfall to the choice of SL and PBL scheme. We show that these sensitivities persist across different lakes and lake-effect storm morphologies. As in their study, we find snowfall differences are mainly due to large differences in F_H and F_Q associated with the formulation of the SL scheme. By using observations we are able to constrain these sensitivities, providing evidence that the schemes producing lower fluxes and lower snowfall are more realistic. As in Conrick et al. (2015), we find QNSE to produce the highest fluxes and snowfall rates as a consequence of its lower assumed value of P_R. However, for the MYJ scheme Conrick et al. (2015) found larger fluxes and snowfall relative to MYNN and attributed it to differences in the formulation of ψ between the schemes. In contrast, we find that the fluxes and snowfall produced by MYJ are only sometimes notably larger than in MYNN (e.g., in Case 2) and that higher fluxes in MYJ are a consequence of a threshold change in thermal roughness that occurs at high u_*.

As in our study, Fujisaki-Manome et al. (2017) found a large variation in simulated F_H and F_Q for a major lake-effect storm. By conducting controlled experiments, only varying the SL and PBL parameterizations, we are able to better quantify the contributions of parameterization uncertainties to these large variations in fluxes. However, other factors, such as differences in analyzed lake conditions and atmospheric boundary forcing, may also play important roles generally, and for the differences found by Fujisaki-Manome et al. (2017). Also, in their study they found that all simulations strongly overestimated peak F_H and F_Q, by over 100 W m^{-2} relative to GLEN observations at Long Point on Lake Erie. In contrast, for Case 1, we find that a majority of schemes

represent peak fluxes quite well, while only a subset of schemes produce strongly excessive fluxes. Some of this difference may be due to bias associated with the inshore water that dominates the fetch of the observations taken at Long Point or imperfect removal of data affected by overland fetch. Where this is less of an issue in the western basin of Lake Erie, the models used by Fujisaki-Manome et al. (2017) performed much better.

7. Conclusions and implications

To investigate the sensitivity of lake-effect snowfall simulations to the parameterization of SL and PBL turbulence we have conducted high-resolution simulations of two major storms, downwind of Lakes Superior and Ontario, using the WRF Model. The simulations included multischeme and parameter sensitivity experiments wherein SL and PBL schemes were altered. High quality measurements of overlake fluxes and downwind snowfall were used to evaluate the simulations. Our primary conclusions are as follows:

- High-resolution numerical simulations of lake-effect snowfall are strongly sensitive to the choice of near-surface turbulence parameterization. This sensitivity is apparent both for events with widespread shallow boundary layer convection and deeper convection with strong mesoscale organization. Simulated precipitation accumulations may differ by up to a factor of 2 depending on the parameterization schemes used.
- Differences between SL schemes are the dominant source of differences in precipitation amounts, through their role in modulating the strength of lake–atmosphere heat and moisture fluxes, and thus the vigor of lake-effect convection. Parameterized surface fluxes vary by over 100 $\mathrm{W\,m^{-2}}$ between SL schemes. The strength of these fluxes is correlated with the amount of precipitation that accumulates downwind of the lake.
- Differences between PBL schemes play a secondary role in modulating the intensity of lake-effect snowfall, though the choice of PBL scheme has notable impacts on storm morphology.
- Most schemes in WRF produce credible simulations of overlake fluxes and downwind snowfall as compared to observations. However, several schemes (QNSE, ACM, TEMF) produce fluxes and precipitation accumulations that are biased substantially high relative to observations.
- For two SL schemes studied in depth, QNSE and MYJ, their anomalously large fluxes can be attributed to parameter choices, specifically: P_R (QNSE) and the threshold u_* used for defining regimes in the over-water surface roughness calculation (QNSE and MYJ). Changes to these parameters can be used to bring the fluxes and precipitation produced by these schemes into better agreement with other schemes and observations.

The above results have implications for operational forecasting of LeS using convection-permitting NWP. In the operational convection-permitting High-Resolution Forecasting System (HREF) version 2.1, different PBL/SL schemes are used for different ensemble members, including MYNN (in the HRRR), MYJ (in the NAM nest, HRW NMMB, and HRW NSSL), and YSU (in the HRW ARW) (e.g., Roberts et al. 2019). Differences in these schemes likely contribute to spread in simulated lake–atmosphere fluxes and precipitation that may affect forecasts. Our results suggest that some of this spread can come from unrealistically large fluxes that may be identified and constrained by observations. Further efforts should be made to characterize biases in parameterized lake–atmosphere interactions in order to constrain and improve SL schemes. Such work could build on our results by considering a larger sample of storm events, by examining other sources of flux observations (e.g., buoy-based measurements and/or airborne measurements), and by examining the relationship to lake processes (e.g., surface waves, lake temperatures, and ice cover).

Multiphysics ensembles such as the HREF, wherein forecasts are produced from ensemble members that use structurally distinct physical parameterizations, can be useful for representing uncertainty in physical processes to aid probabilistic forecasting. However, such ensembles have limitations in terms of their practical implementation (multiple schemes must be maintained and supported) and statistical properties (different ensemble members have distinct climatologies and biases). An alternate approach is to use a single suite of physics parameterizations but with stochastic perturbations that represent uncertainties in the parameterized processes (e.g., Berner et al. 2017). One specific method for doing this is to apply perturbations to specific uncertain parameters within schemes, termed stochastic parameter perturbations (SPP; e.g., Jankov et al. 2017; Ollinaho et al. 2017). Our sensitivity experiments show that targeted perturbations to uncertain parameters within SL schemes can produce differences in fluxes and snowfall as large as the differences across a multiphysics SL/PBL ensemble. Thus, SPP applied to SL schemes may produce meaningful spread in convection-permitting ensemble forecasts of LeS. Further work should investigate the application of SPP in SL and PBL schemes for LeS storms, informed by observational constraints on uncertain parameters.

Acknowledgments. This research was supported by NOAA Grants NA16NWS4680005 and NA19OAR4590136

and by Environment and Climate Change Canada. The data used in this research were provided by the Great Lakes Evaporation Network (GLEN), with data compilation and publication provided by LimnoTech under Award/Contract 10042-400759 from the International Joint Commission (IJC) through a subcontract with the Great Lakes Observing System (GLOS), Project IOOS/GLEN-01. The authors thank Scott Holman and Northern Michigan University for the use of Granite Island Light Station, as well as the Superior Watershed Partnership for access to Stannard Rock lighthouse. The statements, findings, conclusions, and recommendations are those of the authors and do not reflect the views of GLEN, LimnoTech, the IJC, or GLOS. The research benefited from conversations with Scott Miller, Jason Covert, and Robert Fovell. The manuscript was improved by helpful comments from George S. Young and two anonymous reviewers.

Data availability statement: Observational datasets used in this study are available at the locations documented in the included dataset citations. WRF Model source code is available at: https://github.com/wrf-model/WRF. Output from WRF simulations is archived at UAlbany and will be made available upon request.

REFERENCES

Alcott, T. I., and W. J. Steenburgh, 2013: Orographic influences on a Great Salt Lake–effect snowstorm. *Mon. Wea. Rev.*, **141**, 2432–2450, https://doi.org/10.1175/MWR-D-12-00328.1.

——, ——, and N. F. Laird, 2012: Great Salt Lake–effect precipitation: Observed frequency, characteristics, and associated environmental factors. *Wea. Forecasting*, **27**, 954–971, https://doi.org/10.1175/WAF-D-12-00016.1.

Angevine, W. M., H. Jiang, and T. Mauritsen, 2010: Performance of an eddy diffusivity–mass flux scheme for shallow cumulus boundary layers. *Mon. Wea. Rev.*, **138**, 2895–2912, https://doi.org/10.1175/2010MWR3142.1.

Ballentine, R. J., A. J. Stamm, E. E. Chermack, G. P. Byrd, and D. Schleede, 1998: Mesoscale model simulation of the 4–5 January 1995 lake-effect snowstorm. *Wea. Forecasting*, **13**, 893–920, https://doi.org/10.1175/1520-0434(1998)013<0893:MMSOTJ>2.0.CO;2.

Benjamin, S. G., and Coauthors, 2016: A North American hourly assimilation and model forecast cycle: The Rapid Refresh. *Mon. Wea. Rev.*, **144**, 1669–1694, https://doi.org/10.1175/MWR-D-15-0242.1.

Bergmaier, P. T., B. Geerts, L. S. Campbell, and W. J. Steenburgh, 2017: The OWLeS IOP2b lake-effect snowstorm: Dynamics of the secondary circulation. *Mon. Wea. Rev.*, **145**, 2437–2459, https://doi.org/10.1175/MWR-D-16-0462.1.

Berner, J., and Coauthors, 2017: Stochastic parameterization: Toward a new view of weather and climate models. *Bull. Amer. Meteor. Soc.*, **98**, 565–588, https://doi.org/10.1175/BAMS-D-15-00268.1.

Blanken, P. D., C. Spence, N. Hedstrom, and J. D. Lenters, 2011: Evaporation from Lake Superior: 1. Physical controls and processes. *J. Great Lakes Res.*, **37**, 707–716, https://doi.org/10.1016/j.jglr.2011.08.009.

Bougeault, P., and P. Lacarrere, 1989: Parameterization of orography-induced turbulence in a mesobeta–scale model. *Mon. Wea. Rev.*, **117**, 1872–1890, https://doi.org/10.1175/1520-0493(1989)117<1872:POOITI>2.0.CO;2.

Bretherton, C. S., and S. Park, 2009: A new moist turbulence parameterization in the Community Atmosphere Model. *J. Climate*, **22**, 3422–3448, https://doi.org/10.1175/2008JCLI2556.1.

Brown, R. A., T. A. Niziol, N. R. Donaldson, P. I. Joe, and V. T. Wood, 2007: Improved detection using negative elevation angles for mountaintop WSR-88Ds. Part III: Simulations of shallow convective activity over and around Lake Ontario. *Wea. Forecasting*, **22**, 839–852, https://doi.org/10.1175/WAF1019.1.

Burt, C. C., 2007: *Extreme Weather: A Guide & Record Book*. WW Norton & Company, 303 pp.

Campbell, L. S., and W. J. Steenburgh, 2017: The OWLeS IOP2b lake-effect snowstorm: Mechanisms contributing to the Tug Hill precipitation maximum. *Mon. Wea. Rev.*, **145**, 2461–2478, https://doi.org/10.1175/MWR-D-16-0461.1.

——, ——, P. G. Veals, T. W. Letcher, and J. R. Minder, 2016: Lake-effect mode and precipitation enhancement over the Tug Hill Plateau during OWLeS IOP2b. *Mon. Wea. Rev.*, **144**, 1729–1748, https://doi.org/10.1175/MWR-D-15-0412.1.

Chang, S. S., and R. R. Braham Jr., 1991: Observational study of a convective internal boundary layer over Lake Michigan. *J. Atmos. Sci.*, **48**, 2265–2279, https://doi.org/10.1175/1520-0469(1991)048<2265:OSOACI>2.0.CO;2.

Charnock, H., 1955: Wind stress on a water surface. *Quart. J. Roy. Meteor. Soc.*, **81**, 639–640, https://doi.org/10.1002/qj.49708135027.

Ching, J., R. Rotunno, M. LeMone, A. Martilli, B. Kosovic, P. A. Jimenez, and J. Dudhia, 2014: Convectively induced secondary circulations in fine-grid mesoscale numerical weather prediction models. *Mon. Wea. Rev.*, **142**, 3284–3302, https://doi.org/10.1175/MWR-D-13-00318.1.

Chu, P. Y., J. G. Kelley, G. V. Mott, A. Zhang, and G. A. Lang, 2011: Development, implementation, and skill assessment of the NOAA/NOS Great Lakes operational forecast system. *Ocean Dyn.*, **61**, 1305–1316, https://doi.org/10.1007/s10236-011-0424-5.

Cohen, A. E., S. M. Cavallo, M. C. Coniglio, and H. E. Brooks, 2015: A review of planetary boundary layer parameterization schemes and their sensitivity in simulating southeastern U.S. cold season severe weather environments. *Wea. Forecasting*, **30**, 591–612, https://doi.org/10.1175/WAF-D-14-00105.1.

Coniglio, M. C., J. Correia Jr., P. T. Marsh, and F. Kong, 2013: Verification of convection-allowing WRF model forecasts of the planetary boundary layer using sounding observations. *Wea. Forecasting*, **28**, 842–862, https://doi.org/10.1175/WAF-D-12-00103.1.

Conrick, R., H. D. Reeves, and S. Zhong, 2015: The dependence of QPF on the choice of boundary-and surface-layer parameterization for a lake-effect snowstorm. *J. Appl. Meteor. Climatol.*, **54**, 1177–1190, https://doi.org/10.1175/JAMC-D-14-0291.1.

Dyer, A., and B. Hicks, 1970: Flux-gradient relationships in the constant flux layer. *Quart. J. Roy. Meteor. Soc.*, **96**, 715–721, https://doi.org/10.1002/qj.49709641012.

Edson, J. B., and Coauthors, 2013: On the exchange of momentum over the open ocean. *J. Phys. Oceanogr.*, **43**, 1589–1610, https://doi.org/10.1175/JPO-D-12-0173.1.

Eichenlaub, V. L., and T. W. Hodler, 1979: *Weather and Climate of the Great Lakes Region*. University of Notre Dame Press, 335 pp.

Estoque, M., and K. Ninomiya, 1976: Numerical simulation of Japan Sea effect snowfall. *Tellus*, **28**, 243–253, https://doi.org/10.3402/tellusa.v28i3.10285.

Fairall, C., E. F. Bradley, J. Hare, A. Grachev, and J. Edson, 2003: Bulk parameterization of air–sea fluxes: Updates and verification for the COARE algorithm. *J. Climate*, **16**, 571–591, https://doi.org/10.1175/1520-0442(2003)016<0571:BPOASF>2.0.CO;2.

Federal Emergency Management Agency, 2014: New York Severe Winter Storm, Snowstorm, and Flooding (DR-4204). Federal Emergency Management Agency, accessed 6 February 2020, https://www.fema.gov/disaster/4204.

Foken, T., 2006: 50 years of the Monin–Obukhov similarity theory. *Bound.-Layer Meteor.*, **119**, 431–447, https://doi.org/10.1007/s10546-006-9048-6.

Fujisaki-Manome, A., and Coauthors, 2017: Turbulent heat fluxes during an extreme lake-effect snow event. *J. Hydrometeor.*, **18**, 3145–3163, https://doi.org/10.1175/JHM-D-17-0062.1.

García-Díez, M., J. Fernández, L. Fita, and C. Yagüe, 2013: Seasonal dependence of WRF model biases and sensitivity to PBL schemes over Europe. *Quart. J. Roy. Meteor. Soc.*, **139**, 501–514, https://doi.org/10.1002/qj.1976.

Gerbush, M. R., D. A. Kristovich, and N. F. Laird, 2008: Mesoscale boundary layer and heat flux variations over pack ice–covered Lake Erie. *J. Appl. Meteor. Climatol.*, **47**, 668–682, https://doi.org/10.1175/2007JAMC1479.1.

Grell, G. A., and Coauthors, 2014: A scale and aerosol aware stochastic convective parameterization for weather and air quality modeling. *Atmos. Chem. Phys.*, **14**, 5233–5250, https://doi.org/10.5194/acp-14-5233-2014.

Grenier, H., and C. S. Bretherton, 2001: A moist PBL parameterization for large-scale models and its application to subtropical cloud-topped marine boundary layers. *Mon. Wea. Rev.*, **129**, 357–377, https://doi.org/10.1175/1520-0493(2001)129<0357:AMPPFL>2.0.CO;2.

Hjelmfelt, M. R., 1990: Numerical study of the influence of environmental conditions on lake-effect snowstorms over Lake Michigan. *Mon. Wea. Rev.*, **118**, 138–150, https://doi.org/10.1175/1520-0493(1990)118<0138:NSOTIO>2.0.CO;2.

Högström, U., 1996: Review of some basic characteristics of the atmospheric surface layer. *Bound.-Layer Meteor.*, **78**, 215–246, https://doi.org/10.1007/BF00120937.

Hong, S.-Y., Y. Noh, and J. Dudhia, 2006: A new vertical diffusion package with an explicit treatment of entrainment processes. *Mon. Wea. Rev.*, **134**, 2318–2341, https://doi.org/10.1175/MWR3199.1.

Iacono, M. J., J. S. Delamere, E. J. Mlawer, M. W. Shephard, S. A. Clough, and W. D. Collins, 2008: Radiative forcing by long-lived greenhouse gases: Calculations with the AER radiative transfer models. *J. Geophys. Res.*, **113**, D13103, https://doi.org/10.1029/2008JD009944.

Janjić, Z., 1994: The step-mountain eta coordinate model: Further developments of the convection, viscous sublayer, and turbulence closure schemes. *Mon. Wea. Rev.*, **122**, 927–945, https://doi.org/10.1175/1520-0493(1994)122<0927:TSMECM>2.0.CO;2.

——, 2001: Nonsingular implementation of the Mellor-Yamada level 2.5 scheme in the NCEP Meso model. NCEP Office Note 437, 61 pp.

Jankov, I., and Coauthors, 2017: A performance comparison between multiphysics and stochastic approaches within a North American RAP ensemble. *Mon. Wea. Rev.*, **145**, 1161–1179, https://doi.org/10.1175/MWR-D-16-0160.1.

Jiménez, P. A., J. Dudhia, J. F. González-Rouco, J. Navarro, J. P. Montávez, and E. García-Bustamante, 2012: A revised scheme for the WRF surface layer formulation. *Mon. Wea. Rev.*, **140**, 898–918, https://doi.org/10.1175/MWR-D-11-00056.1.

Kindap, T., 2010: A severe sea-effect snow episode over the city of Istanbul. *Nat. Hazards*, **54**, 707–723, https://doi.org/10.1007/s11069-009-9496-7.

Kristovich, D. A., 1993: Mean circulations of boundary-layer rolls in lake-effect snow storms. *Bound.-Layer Meteor.*, **63**, 293–315, https://doi.org/10.1007/BF00710463.

——, N. F. Laird, and M. R. Hjelmfelt, 2003: Convective evolution across Lake Michigan during a widespread lake-effect snow event. *Mon. Wea. Rev.*, **131**, 643–655, https://doi.org/10.1175/1520-0493(2003)131<0643:CEALMD>2.0.CO;2.

——, and Coauthors, 2017: The Ontario Winter Lake-effect Systems field campaign: Scientific and educational adventures to further our knowledge and prediction of lake-effect storms. *Bull. Amer. Meteor. Soc.*, **98**, 315–332, https://doi.org/10.1175/BAMS-D-15-00034.1.

Laird, N., R. Sobash, and N. Hodas, 2009: The frequency and characteristics of lake-effect precipitation events associated with the New York State Finger Lakes. *J. Appl. Meteor. Climatol.*, **48**, 873–886, https://doi.org/10.1175/2008JAMC2054.1.

——, A. M. Bentley, S. A. Ganetis, A. Stieneke, and S. A. Tushaus, 2016: Climatology of lake-effect precipitation events over Lake Tahoe and Pyramid Lake. *J. Appl. Meteor. Climatol.*, **55**, 297–312, https://doi.org/10.1175/JAMC-D-14-0230.1.

——, N. D. Metz, L. Gaudet, C. Grasmick, L. Higgins, C. Loeser, and D. A. Zelinsky, 2017: Climatology of cold season lake-effect cloud bands for the North American Great Lakes. *Int. J. Climatol.*, **37**, 2111–2121, https://doi.org/10.1002/joc.4838.

LeMone, M. A., 1973: The structure and dynamics of horizontal roll vortices in the planetary boundary layer. *J. Atmos. Sci.*, **30**, 1077–1091, https://doi.org/10.1175/1520-0469(1973)030<1077:TSADOH>2.0.CO;2.

Lenschow, D., 1973: Two examples of planetary boundary layer modification over the Great Lakes. *J. Atmos. Sci.*, **30**, 568–581, https://doi.org/10.1175/1520-0469(1973)030<0568:TEOPBL>2.0.CO;2.

Li, D., 2019: Turbulent Prandtl number in the atmospheric boundary layer—Where are we now? *Atmos. Res.*, **216**, 86–105, https://doi.org/10.1016/j.atmosres.2018.09.015.

Maesaka, T., G. K. Moore, Q. Liu, and K. Tsuboki, 2006: A simulation of a lake effect snowstorm with a cloud resolving numerical model. *Geophys. Res. Lett.*, **33**, L20813, https://doi.org/10.1029/2006GL026638.

McMillen, J. D., and W. J. Steenburgh, 2015a: Capabilities and limitations of convection-permitting WRF simulations of lake-effect systems over the Great Salt Lake. *Wea. Forecasting*, **30**, 1711–1731, https://doi.org/10.1175/WAF-D-15-0017.1.

——, and ——, 2015b: Impact of microphysics parameterizations on simulations of the 27 October 2010 Great Salt Lake–effect snowstorm. *Wea. Forecasting*, **30**, 136–152, https://doi.org/10.1175/WAF-D-14-00060.1.

Mellor, G., and T. Yamada, 1982: Development of a turbulence closure-model for geophysical fluid problems. *Rev. Geophys.*, **20**, 851–875, https://doi.org/10.1029/RG020i004p00851.

Menne, M. J., I. Durre, R. S. Vose, B. E. Gleason, and T. G. Houston, 2012a: An overview of the global historical climatology network-daily database. *J. Atmos. Oceanic Technol.*, **29**, 897–910, https://doi.org/10.1175/JTECH-D-11-00103.1.

——, and Coauthors, 2012b: Global Historical Climatology Network-Daily (GHCN-Daily), version 3. NOAA National Climatic Data Center, accessed 24 August 2018, https://doi.org/10.7289/V5D21VHZ.

Milovac, J., K. Warrach-Sagi, A. Behrendt, F. Späth, J. Ingwersen, and V. Wulfmeyer, 2016: Investigation of PBL schemes combining the WRF model simulations with scanning water vapor differential absorption lidar measurements. *J. Geophys. Res. Atmos.*, **121**, 624–649, https://doi.org/10.1002/2015JD023927.

Minder, J. R., T. W. Letcher, L. S. Campbell, P. G. Veals, and W. J. Steenburgh, 2015: The evolution of lake-effect convection during landfall and orographic uplift as observed by profiling radars. *Mon. Wea. Rev.*, **143**, 4422–4442, https://doi.org/10.1175/MWR-D-15-0117.1.

Monin, A., and A. Obukhov, 1954: Basic laws of turbulent mixing in the surface layer of the atmosphere. *Tr. Geofiz. Inst., Akad. Nauk SSSR*, **24**, 163–187.

Mulholland, J. P., J. Frame, S. W. Nesbitt, S. M. Steiger, K. A. Kosiba, and J. Wurman, 2017: Observations of misovortices within a long-lake-axis-parallel lake-effect snowband during the OWLeS project. *Mon. Wea. Rev.*, **145**, 3265–3291, https://doi.org/10.1175/MWR-D-16-0430.1.

Nakanishi, M., and H. Niino, 2004: An improved Mellor–Yamada level-3 model with condensation physics: Its design and verification. *Bound.-Layer Meteor.*, **112**, 1–31, https://doi.org/10.1023/B:BOUN.0000020164.04146.98.

——, and ——, 2009: Development of an improved turbulence closure model for the atmospheric boundary layer. *J. Meteor. Soc. Japan*, **87**, 895–912, https://doi.org/10.2151/JMSJ.87.895.

Niziol, T. A., W. R. Snyder, and J. S. Waldstreicher, 1995: Winter weather forecasting throughout the eastern United States. Part IV: Lake-effect snow. *Wea. Forecasting*, **10**, 61–77, https://doi.org/10.1175/1520-0434(1995)010<0061:WWFTTE>2.0.CO;2.

NOAA/NWS Radar Operations Center, 1991: NOAA Next Generation Radar (NEXRAD) Level 2 Base Data. NOAA/National Centers for Environmental Information, accessed 6 March 2018, https://doi.org/10.7289/V5W9574V.

NOAA/NCEP, 2004: North American Mesoscale Forecast System (NAM) analyses, continuing from March 2004 (updated daily). NOAA/National Centers for Environmental Information (NCEI), https://nomads.ncdc.noaa.gov/data/namanl/.

——, 2012: Rapid Refresh (RAP) operational model output, continuing from July 2012 (updated daily). NOAA/National Centers for Environmental Information (NCEI), https://nomads.ncdc.noaa.gov/data/rap130/.

NOAA/NOS, 2005: Great Lakes Operational Forecast System, nowcast. Great Lakes Observing System (GLOS), http://tds.glos.us/thredds/catalog/glcfs/glcfs_nowcast.html.

Ollinaho, P., and Coauthors, 2017: Towards process-level representation of model uncertainties: Stochastically perturbed parametrizations in the ECMWF ensemble. *Quart. J. Roy. Meteor. Soc.*, **143**, 408–422, https://doi.org/10.1002/qj.2931.

Pleim, J. E., 2006: A simple, efficient solution of flux–profile relationships in the atmospheric surface layer. *J. Appl. Meteor. Climatol.*, **45**, 341–347, https://doi.org/10.1175/JAM2339.1.

——, 2007: A combined local and nonlocal closure model for the atmospheric boundary layer. Part I: Model description and testing. *J. Appl. Meteor. Climatol.*, **46**, 1383–1395, https://doi.org/10.1175/JAM2539.1.

Rasmussen, R., and Coauthors, 2012: How well are we measuring snow: The NOAA/FAA/NCAR winter precipitation test bed. *Bull. Amer. Meteor. Soc.*, **93**, 811–829, https://doi.org/10.1175/BAMS-D-11-00052.1.

Reeves, H. D., and D. T. Dawson, 2013: The dependence of QPF on the choice of microphysical parameterization for lake-effect snowstorms. *J. Appl. Meteor. Climatol.*, **52**, 363–377, https://doi.org/10.1175/JAMC-D-12-019.1.

Roberts, B., I. L. Jirak, A. J. Clark, S. J. Weiss, and J. S. Kain, 2019: Postprocessing and visualization techniques for convection-allowing ensembles. *Bull. Amer. Meteor. Soc.*, **100**, 1245–1258, https://doi.org/10.1175/BAMS-D-18-0041.1.

Saslo, S., and S. J. Greybush, 2017: Prediction of lake-effect snow using convection-allowing ensemble forecasts and regional data assimilation. *Wea. Forecasting*, **32**, 1727–1744, https://doi.org/10.1175/WAF-D-16-0206.1.

Shao, C., and Coauthors, 2015: Diurnal to annual changes in latent, sensible heat, and CO_2 fluxes over a Laurentian Great Lake: A case study in western Lake Erie. *J. Geophys. Res. Biogeosci.*, **120**, 1587–1604, https://doi.org/10.1002/2015JG003025.

Shin, H. H., and S.-Y. Hong, 2015: Representation of the subgrid-scale turbulent transport in convective boundary layers at gray-zone resolutions. *Mon. Wea. Rev.*, **143**, 250–271, https://doi.org/10.1175/MWR-D-14-00116.1.

Skamarock, W.C., and Coauthors, 2008: A description of the Advanced Research WRF version 3. NCAR Tech. Note NCAR/TN-475+STR, 113 pp., https://doi.org/10.5065/D68S4MVH.

Smirnova, T. G., J. M. Brown, S. G. Benjamin, and J. S. Kenyon, 2016: Modifications to the Rapid Update Cycle Land Surface Model (RUC LSM) available in the Weather Research and Forecasting (WRF) Model. *Mon. Wea. Rev.*, **144**, 1851–1865, https://doi.org/10.1175/MWR-D-15-0198.1.

Spence, C., P. Blanken, J. Lenters, and N. Hedstrom, 2013: The importance of spring and autumn atmospheric conditions for the evaporation regime of Lake Superior. *J. Hydrometeor.*, **14**, 1647–1658, https://doi.org/10.1175/JHM-D-12-0170.1.

——, N. Hedstrom, P. D. Blanken, J. Lenters, and G. J. Cutrell, 2019: Great Lakes Evaporation Network (GLEN) data. Great Lakes Observing System (GLOS), accessed 30 December 2019, http://tds.glos.us/thredds/catalog/glos/glen/catalog.html.

Steenburgh, W. J., and D. J. Onton, 2001: Multiscale analysis of the 7 December 1998 Great Salt Lake–effect snowstorm. *Mon. Wea. Rev.*, **129**, 1296–1317, https://doi.org/10.1175/1520-0493(2001)129<1296:MAOTDG>2.0.CO;2.

——, and L. S. Campbell, 2017: The OWLeS IOP2b lake-effect snowstorm: Shoreline geometry and the mesoscale forcing of precipitation. *Mon. Wea. Rev.*, **145**, 2421–2436, https://doi.org/10.1175/MWR-D-16-0460.1.

——, L. Campbell, and P. Veals, 2014a: North Redfield snow study station data, version 1.0. UCAR/NCAR–Earth Observing Laboratory, https://doi.org/doi:10.5065/D68051CN.

——, ——, and ——, 2014b: Sandy Creek snow study station data, version 1.0. UCAR/NCAR–Earth Observing Laboratory, https://doi.org/10.5065/D68K77WG.

Sukoriansky, S., B. Galperin, and V. Perov, 2005: Application of a new spectral theory of stably stratified turbulence to the atmospheric boundary layer over sea ice. *Bound.-Layer Meteor.*, **117**, 231–257, https://doi.org/10.1007/s10546-004-6848-4.

Thompson, G., and T. Eidhammer, 2014: A study of aerosol impacts on clouds and precipitation development in a large winter cyclone. *J. Atmos. Sci.*, **71**, 3636–3658, https://doi.org/10.1175/JAS-D-13-0305.1.

——, P. Field, R. Rasmussen, and W. Hall, 2008: Explicit forecasts of winter precipitation using an improved bulk microphysics scheme. Part II: Implementation of a new snow parameterization. *Mon. Wea. Rev.*, **136**, 5095–5115, https://doi.org/10.1175/2008MWR2387.1.

Tripoli, G. J., 2005: Numerical study of the 10 January 1998 lake-effect bands observed during Lake-ICE. *J. Atmos. Sci.*, **62**, 3232–3249, https://doi.org/10.1175/JAS3462.1.

Veals, P. G., and W. J. Steenburgh, 2015: Climatological characteristics and orographic enhancement of lake-effect precipitation east of Lake Ontario and over the Tug Hill Plateau. *Mon. Wea. Rev.*, **143**, 3591–3609, https://doi.org/10.1175/MWR-D-15-0009.1.

Vermette, S., 2015: Enough already! Buffalo's Snowvember. *Weatherwise*, **68**, 34–39, https://doi.org/10.1080/00431672.2015.1045369.

Weckwerth, T. M., J. W. Wilson, R. M. Wakimoto, and N. A. Crook, 1997: Horizontal convective rolls: Determining the environmental conditions supporting their existence and characteristics. *Mon. Wea. Rev.*, **125**, 505–526, https://doi.org/10.1175/1520-0493(1997)125<0505:HCRDTE>2.0.CO;2.

Welsh, D., B. Geerts, X. Jing, P. T. Bergmaier, J. R. Minder, W. J. Steenburgh, and L. S. Campbell, 2016: Understanding heavy lake-effect snowfall: The vertical structure of radar reflectivity in a deep snowband over and downwind of Lake Ontario. *Mon. Wea. Rev.*, **144**, 4221–4244, https://doi.org/10.1175/MWR-D-16-0057.1.

Wright, D. M., D. J. Posselt, and A. L. Steiner, 2013: Sensitivity of lake-effect snowfall to lake ice cover and temperature in the Great Lakes region. *Mon. Wea. Rev.*, **141**, 670–689, https://doi.org/10.1175/MWR-D-12-00038.1.

Zhao, L., J. Jin, S.-Y. Wang, and M. B. Ek, 2012: Integration of remote-sensing data with WRF to improve lake-effect precipitation simulations over the Great Lakes region. *J. Geophys. Res.*, **117**, D09102, https://doi.org/10.1029/2011JD016979.